

The Mechanical Threshold Stress model for various tempers of AISI 4340 steel

Biswajit Banerjee¹

Department of Mechanical Engineering, University of Utah, Salt Lake City, UT 84112, USA

Abstract

Numerical simulations of high-strain-rate and high-temperature deformation of pure metals and alloys require realistic plastic constitutive models. Empirical models include the widely used Johnson-Cook model and the semi-empirical Steinberg-Cochran-Guinan-Lund model. Physically based models such as the Zerilli-Armstrong model, the Mechanical Threshold Stress model, and the Preston-Tonks-Wallace model are also coming into wide use. In this paper, we determine the Mechanical Threshold Stress model parameters for various tempers of AISI 4340 steel using experimental data gleaned from the open literature. We compare stress-strain curves and Taylor impact test profiles predicted by the Mechanical Threshold Stress model with those from the Johnson-Cook model for 4340 steel. In addition, temperature- and pressure-dependent shear modulus models, melting temperature models, and a specific heat model for 4340 steel that are needed for such numerical simulations are also described.

1 Introduction

The present work was motivated by the requirement of numerically simulating the deformation and fragmentation of a heated AISI 4340 steel cylinder loaded by explosive deflagration. Such simulations require a plastic constitutive model that is valid over temperatures ranging from 250 K to 1300 K and over strain rates ranging from quasistatic to the order of 10^5 /s. The Mechanical Threshold Stress (MTS) model (Follansbee and Kocks [12], Kocks [27]) is a physically-based model that can be used for the range of temperatures and strain rates of interest in these simulations. In the absence of any MTS models specifically for 4340 steels, an existing

¹ Funded the by U.S. Department of Energy through the Center for the Simulation of Accidental Fires and Explosions, University of Utah

MTS model for HY-100 steel (Goto et al. [14, 15]) was initially explored as a surrogate for 4340 steel. However, the HY-100 model failed to produce results that were in agreement with experimental stress-strain data for 4340 steel. This paper attempts to redress that lacuna by providing the MTS parameters for a number of tempers of 4340 steel (classified by their Rockwell C hardness number). The MTS model is compared with the Johnson-Cook (JC) model (Johnson and Cook [23, 24]) for 4340 steel and the relative advantages and disadvantages of these models are discussed.

The MTS model requires a temperature and pressure dependent elastic shear modulus. We describe a number of shear modulus models and the associated melting temperature models. Conversion of plastic work into heat is achieved through a specific heat model that takes the transformation from the bcc (α) phase to the fcc (γ) phase into account.

2 Models

In this section, we describe the MTS and JC plastic flow stress models. In addition, we present the submodels that are required by the flow stress models: the Mie-Grüneisen (MG) equation of state for calculating the pressure, the Steinberg-Cochran-Guinan (SCG) and Burakovsky-Preston-Silbar (BPS) melting temperature models, and the Chen-Gray (MTS), the Steinberg-Guinan (SG), and the Nadal-LePoac (NP) shear modulus models. More details about the models may be found in the cited references.

2.1 MTS Flow Stress Model

The Mechanical Threshold Stress (MTS) model (Follansbee and Kocks [12], Goto et al. [15]) gives the following form for the flow stress

$$\sigma_y(\epsilon_p, \dot{\epsilon}, T) = \sigma_a + (S_i \sigma_i + S_e \sigma_e) \frac{\mu(p, T)}{\mu_0} \quad (1)$$

where σ_y is the flow stress, ϵ_p is the plastic strain, $\dot{\epsilon}$ is the strain rate, T is the temperature, σ_a is the athermal component of mechanical threshold stress, μ_0 is the shear modulus at 0 K and ambient pressure, σ_i is the intrinsic component of the flow stress due to barriers to thermally activated dislocation motion, σ_e is the strain hardening component of the flow stress. The scaling factors S_i and S_e are

temperature and strain rate dependent and take the Arrhenius form

$$S_i = \left[1 - \left(\frac{k_b T}{g_{0i} b^3 \mu(p, T)} \ln \frac{\dot{\epsilon}_{0i}}{\dot{\epsilon}} \right)^{1/q_i} \right]^{1/p_i} \quad (2)$$

$$S_e = \left[1 - \left(\frac{k_b T}{g_{0e} b^3 \mu(p, T)} \ln \frac{\dot{\epsilon}_{0e}}{\dot{\epsilon}} \right)^{1/q_e} \right]^{1/p_e} \quad (3)$$

where k_b is the Boltzmann constant, b is the magnitude of the Burgers' vector, (g_{0i}, g_{0e}) are normalized activation energies, $(\dot{\epsilon}_{0i}, \dot{\epsilon}_{0e})$ are constant reference strain rates, and (q_i, p_i, q_e, p_e) are constants. The strain hardening component of the mechanical threshold stress (σ_e) is given by a modified Voce law

$$\frac{d\sigma_e}{d\epsilon_p} = \theta(\sigma_e) \quad (4)$$

where

$$\theta(\sigma_e) = \theta_0 [1 - F(\sigma_e)] + \theta_1 F(\sigma_e) \quad (5)$$

$$\theta_0 = a_{00} + a_{10} \ln \dot{\epsilon} + a_{20} \sqrt{\dot{\epsilon}} + a_{30} T \quad (6)$$

$$\theta_1 = a_{01} + a_{11} \ln \dot{\epsilon} + a_{21} \sqrt{\dot{\epsilon}} + a_{31} T \quad (7)$$

$$F(\sigma_e) = \frac{\tanh\left(\alpha \frac{\sigma_e}{\sigma_{es}}\right)}{\tanh(\alpha)} \quad (8)$$

$$\ln\left(\frac{\sigma_{es}}{\sigma_{0es}}\right) = \left(\frac{k_b T}{g_{0es} b^3 \mu(p, T)} \right) \ln\left(\frac{\dot{\epsilon}}{\dot{\epsilon}_{0es}}\right) \quad (9)$$

and θ_0 is the hardening due to dislocation accumulation, θ_1 can be thought of as the contribution due to stage-IV hardening, $(a_{0j}, a_{1j}, a_{2j}, a_{3j}, \alpha)$ are constants ($j = 0, 1$), σ_{es} is the stress at zero strain hardening rate, σ_{0es} is the saturation threshold stress for deformation at 0 K, g_{0es} is a constant, and $\dot{\epsilon}_{0es}$ is the maximum strain rate. Note that the maximum strain rate for which the model is valid is usually limited to about $10^7/s$.

2.2 JC Flow Stress Model

The Johnson-Cook (JC) model (Johnson and Cook [23]) is purely empirical and has the form

$$\sigma_y(\epsilon_p, \dot{\epsilon}, T) = \sigma_0 \left[1 + \frac{B}{\sigma_0} (\epsilon_p)^n \right] [1 + C \ln(\dot{\epsilon}^*)] [1 - (T^*)^m] \quad (10)$$

where ϵ_p is the equivalent plastic strain, $\dot{\epsilon}$ is the plastic strain rate, (σ_0, B, C, n, m) are material constants,

$$\dot{\epsilon}^* = \frac{\dot{\epsilon}}{\dot{\epsilon}_0}; \quad T^* = \frac{(T - T_r)}{(T_m - T_r)}, \quad (11)$$

$\dot{\epsilon}_0$ is a reference strain rate, T_r is a reference temperature, and T_m is the melt temperature.

2.3 Mie-Grüneisen Equation of State

The hydrostatic pressure (p) is calculated using a temperature-corrected Mie-Grüneisen equation of state of the form (Zocher et al. [43], see also Wilkins [40], p. 61)

$$p = \frac{\rho_0 C_0^2 (\eta - 1) \left[\eta - \frac{\Gamma_0}{2} (\eta - 1) \right]}{[\eta - S_\alpha (\eta - 1)]^2} + \Gamma_0 E; \quad \eta = \frac{\rho}{\rho_0} \quad (12)$$

where C_0 is the bulk speed of sound, ρ_0 is the initial density, ρ is the current density, Γ_0 is the Grüneisen's gamma at reference state, $S_\alpha = dU_s/dU_p$ is a linear Hugoniot slope coefficient, U_s is the shock wave velocity, U_p is the particle velocity, and E is the internal energy per unit reference specific volume. The internal energy is computed using

$$E = \frac{1}{V_0} \int C_v dT \approx \frac{C_v (T - T_0)}{V_0} \quad (13)$$

where $V_0 = 1/\rho_0$ is the reference specific volume at temperature $T = T_0$, and C_v is the specific heat at constant volume.

2.4 SCG Melting Temperature Model

The Steinberg-Cochran-Guinan (SCG) melting temperature model (Steinberg et al. [36]) is based on a modified Lindemann law and has the form

$$T_m(\rho) = T_{m0} \exp \left[2a \left(1 - \frac{1}{\eta} \right) \right] \eta^{2(\Gamma_0 - a - 1/3)}; \quad \eta = \frac{\rho}{\rho_0} \quad (14)$$

where T_m is the melting temperature, T_{m0} is the melt temperature at $\eta = 1$, a is the coefficient of the first order volume correction to Grüneisen's gamma (Γ_0).

2.5 BPS Melting Temperature Model

An alternative melting relation that is based on dislocation-mediated phase transitions is the the Burakovsky-Preston-Silbar (BPS) model (Burakovsky et al. [8]).

The BPS model has the form

$$T_m(p) = T_m(0) \left[\frac{1}{\eta} + \frac{1}{\eta^{4/3}} \frac{\mu'_0}{\mu_0} p \right]; \quad \eta = \left(1 + \frac{K'_0}{K_0} p \right)^{1/K'_0} \quad (15)$$

$$T_m(0) = \frac{\kappa \lambda \mu_0 v_{WS}}{8\pi \ln(z-1) k_b} \ln \left(\frac{\alpha^2}{4 b^2 \rho_c(T_m)} \right) \quad (16)$$

where p is the pressure, $\eta = \rho/\rho_0$ is the compression, μ_0 is the shear modulus at room temperature and zero pressure, $\mu'_0 = \partial\mu/\partial p$ is the derivative of the shear modulus at zero pressure, K_0 is the bulk modulus at room temperature and zero pressure, $K'_0 = \partial K/\partial p$ is the derivative of the bulk modulus at zero pressure, κ is a constant, $\lambda = b^3/v_{WS}$ where b is the magnitude of the Burgers' vector, v_{WS} is the Wigner-Seitz volume, z is the coordination number, α is a constant, $\rho_c(T_m)$ is the critical density of dislocations, and k_b is the Boltzmann constant.

2.6 MTS Shear Modulus Model

The Chen-Gray (MTS) shear modulus model has been used in conjunction with the MTS plasticity model by Goto et al. [15]. This model is of the form (Varshni [38], Chen and Gray [10])

$$\mu(T) = \mu_0 - \frac{D}{\exp(T_0/T) - 1} \quad (17)$$

where μ_0 is the shear modulus at 0K, and D, T_0 are material constants.

2.7 SCG Shear Modulus Model

The Steinberg-Cochran-Guinan (SCG) shear modulus model (Steinberg et al. [36], Zocher et al. [43]) is pressure dependent and has the form

$$\mu(p, T) = \mu_0 + \frac{\partial\mu}{\partial p} \frac{p}{\eta^{1/3}} + \frac{\partial\mu}{\partial T} (T - 300); \quad \eta = \rho/\rho_0 \quad (18)$$

where, μ_0 is the shear modulus at the reference state ($T = 300$ K, $p = 0$, $\eta = 1$), p is the pressure, and T is the temperature. When the temperature is above T_m , the shear modulus is instantaneously set to zero in this model.

2.8 NP Shear Modulus Model

A modified version of the SCG model has been developed by Nadal and Le Poac [32] that attempts to capture the sudden drop in the shear modulus close to the

melting temperature in a smooth manner. The Nadal-LePoac (NP) shear modulus model has the form

$$\mu(p, T) = \frac{1}{\mathcal{J}(\hat{T})} \left[\left(\mu_0 + \frac{\partial \mu}{\partial p} \frac{p}{\eta^{1/3}} \right) (1 - \hat{T}) + \frac{\rho}{Cm} k_b T \right]; \quad C := \frac{(6\pi^2)^{2/3}}{3} f^2 \quad (19)$$

where

$$\mathcal{J}(\hat{T}) := 1 + \exp \left[-\frac{1 + 1/\zeta}{1 + \zeta/(1 - \hat{T})} \right] \quad \text{for} \quad \hat{T} := \frac{T}{T_m} \in [0, 1 + \zeta], \quad (20)$$

μ_0 is the shear modulus at 0 K and ambient pressure, ζ is a material parameter, k_b is the Boltzmann constant, m is the atomic mass, and f is the Lindemann constant.

2.9 Adiabatic Heating and Specific Heat Model

A part of the plastic work done is converted into heat and used to update the temperature. The increase in temperature (ΔT) due to an increment in plastic strain ($\Delta \epsilon_p$) is given by the equation

$$\Delta T = \frac{\chi \sigma_y}{\rho C_p} \Delta \epsilon_p \quad (21)$$

where χ is the Taylor-Quinney coefficient, and C_p is the specific heat. The value of the Taylor-Quinney coefficient is taken to be 0.9 in all our simulations (see Ravichandran et al. [34] for more details on the variation of χ with strain and strain rate).

A relation for the dependence of C_p upon temperature is used for the steel (Lederman et al. [29]).

$$C_p = \begin{cases} A_1 + B_1 t + C_1 |t|^{-\alpha} & \text{if } T < T_c \\ A_2 + B_2 t + C_2 t^{-\alpha'} & \text{if } T > T_c \end{cases} \quad (22)$$

$$t = \frac{T}{T_c} - 1 \quad (23)$$

where T_c is the critical temperature at which the phase transformation from the α to the γ phase takes place, and $A_1, A_2, B_1, B_2, \alpha, \alpha'$ are constants.

3 Submodel Parameters and Validation

The shear modulus, melting temperature, equation of state, and specific heat models affect the accuracy of the MTS model predictions. We have used the BPS melting

temperature model, the NP shear modulus model, the Mie-Grüneisen equation of state, and the Lederman specific heat models in the process of determining the MTS model parameters and subsequent simulations. We verify the accuracy of these models in this section and present the parameters used. Note that some of these parameters are new and have been determined so as to fit the experimental data.

3.1 Shear Modulus Models for 4340 Steel

The parameters used in the shear modulus models are shown in Table 1. The parameters for the MTS model have been obtained from a least square fit to the data at a compression of 1. The values of μ_0 and $\partial\mu/\partial p$ for the SCG model are from Guinan and Steinberg [16]. The derivative with respect to temperature has been chosen so as to fit the data at a compression of 1. The NP shear model parameters μ_0 and C have also been chosen to fit the data. A value of 0.57 for C is suggested by Nadal and Le Poac [32]. However, this value leads to a higher value of μ at high temperatures.

Figure 1 shows the performance of the three models for three values of compression. The melting temperature is determined using the BPS model discussed earlier. The initial density is taken to be 7830 kg/m^3 . The MTS model shows no pressure dependence of the shear modulus unless the melting temperature is computed as a function of pressure. However, the model behaves well at low temperatures for $\eta = 1$. Both the SCG and NP shear modulus models are pressure dependent and provide a good fit to the data. We have used the NP shear modulus model for subsequent calculations for 4340 steel because of its smooth transition to zero modulus at melt.

Table 1
Parameters used in shear modulus models for 4340 steel.

MTS shear modulus model				
μ_0 (GPa)	D (GPa)	T_0 (K)		
85.0	10.0	298		
SCG shear modulus model				
μ_0 (GPa)	$\partial\mu/\partial p$	$\partial\mu/\partial T$ (GPa/K)		
81.9	1.8	0.0387		
NP shear modulus model				
μ_0 (GPa)	$\partial\mu/\partial p$	ζ	C	m (amu)
90.0	1.8	0.04	0.080	55.947

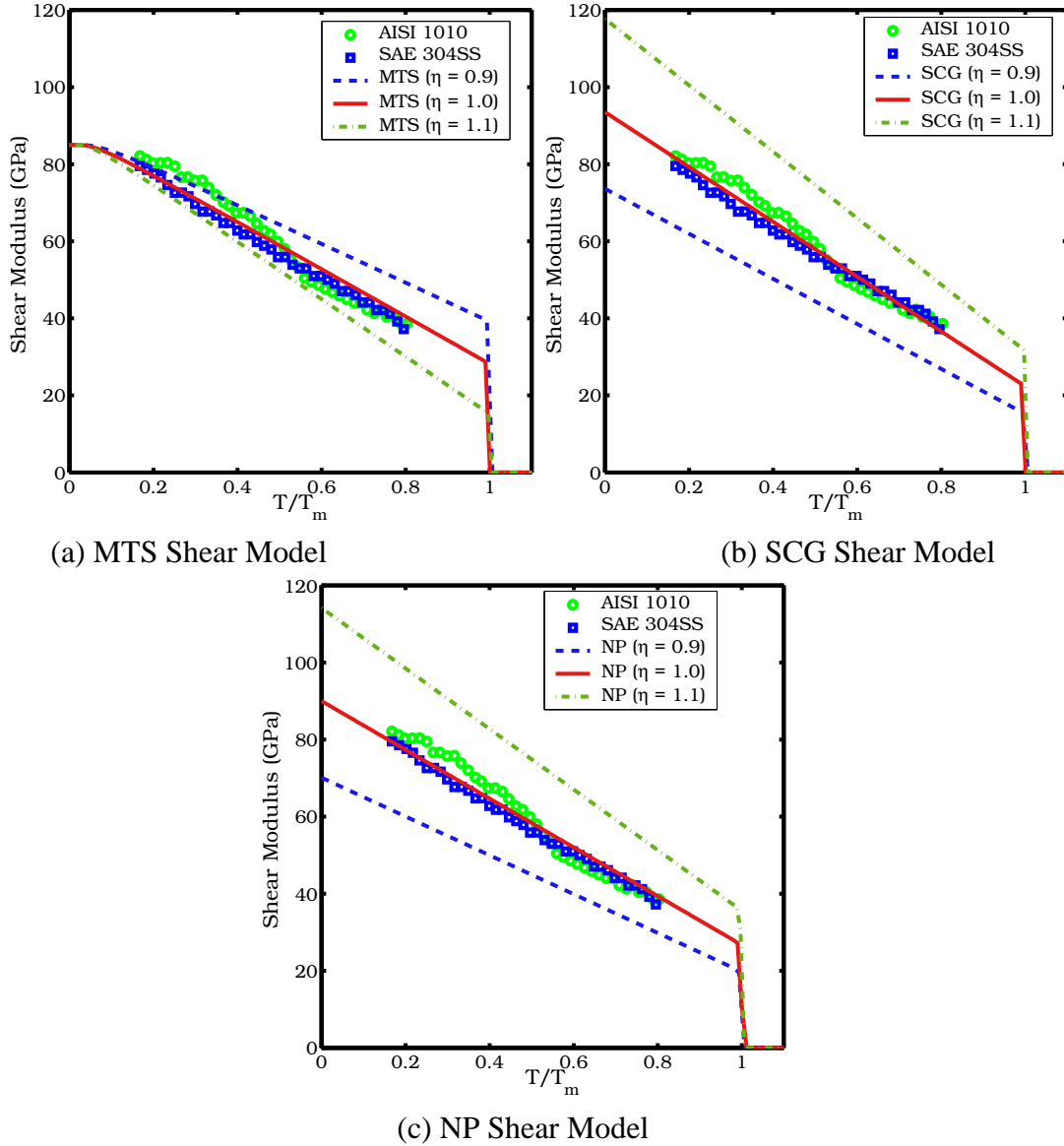


Fig. 1. Comparison of experimental data with model predictions of shear modulus for 4340 steel. The experimental data are for AISI 1010 steel and SAE 304 stainless steel (Fukuhara and Sanpei [13]).

3.2 Melting Temperature Model for 4340 Steel

Figure 2 shows a comparison of the predictions from the SCG (Equation 14) and BPS (Equation 15) models with experimental data for iron from Burakovsky et al. [8] (includes data from Williams et al. [41] and Yoo et al. [42]). The BPS model performs better at high pressures, but both models are within experimental variability below 100 GPa. The parameters used in the models are shown in Table 2. The bulk and shear moduli and their derivatives for iron have been obtained from Guinan and Steinberg [16]. The parameters for the BPS model at zero pressure

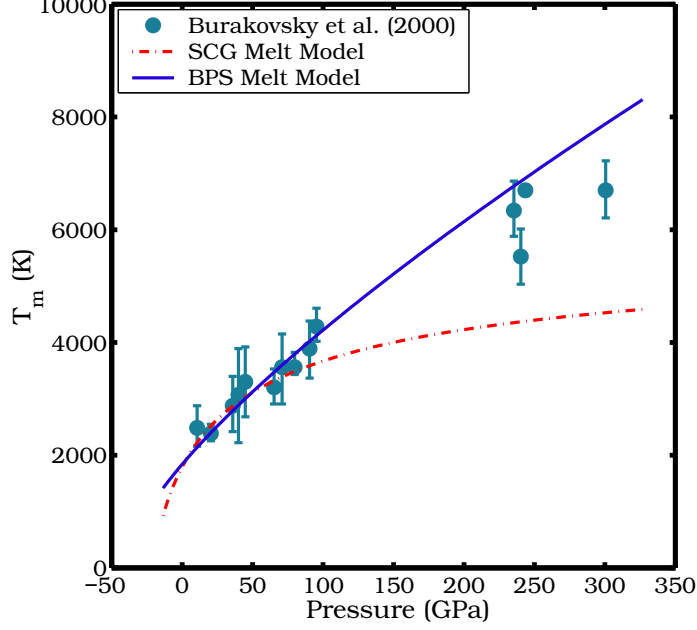


Fig. 2. Comparison of experimental data and model predictions of melting temperature for 4340 steel as a function of pressure.

have been obtained from Burakovsky and Preston [7] and Burakovsky et al. [9], and the lattice constant (a) has been taken from Jansen et al. [22]. The SCG model parameters have been obtained from Gust [17]. An initial density ρ_0 of 7830 kg/m³ has been used in the model calculations.

3.3 Equation of State for 4340 Steel

The pressure in the steel is calculated using the Mie-Grüneisen equation of state (equation 12) assuming a linear Hugoniot relation. The Grüneisen gamma (Γ_0) is assumed to be a constant over the regime of interest. The specific heat at constant volume is assumed to be the same as that at constant pressure and is calculated using equation (22). Table 3 shows the parameters used in the pressure calculation. The

Table 2

Parameters used in melting temperature models for 4340 steel.

Steinberg-Cochran-Guinan (SCG) model											
$T_{m0}(K)$	Γ_0	a									
1793	1.67	1.67									
Burakovsky-Preston-Silbar (BPS) model											
K_0 (GPa)	K'_0	μ_0 (GPa)	μ'_0	κ	z	$b^2\rho_c(T_m)$	α	λ	v_{WS} (Å ³)	a (Å)	
166	5.29	81.9	1.8	1	8	0.78	2.9	1.30	$a^3/2$	2.865	

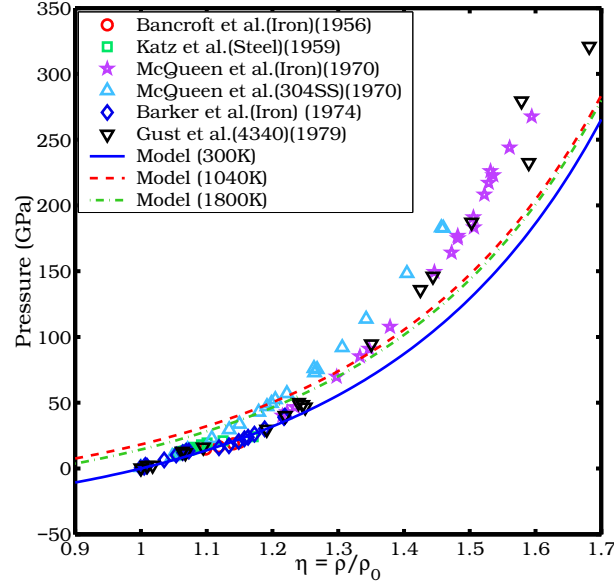


Fig. 3. Comparison of experimental data with model predictions of equation of state for 4340 steel.

bulk speed of sound and the linear Hugoniot slope coefficient have been obtained from Brown et al. [5] for iron. The Grüneisen gamma value has been interpolated from the values given by Gust et al. [18]. An initial temperature (T_0) of 300 K and an initial density of 7830 kg/m^3 have been used in the model calculations.

Figure 3 compares model predictions with experimental data for iron (Bancroft et al. [1], McQueen et al. [31], Barker and Hollenbach [4]), mild steel (Katz et al. [26]), 300 series stainless steels (McQueen et al. [31]), and for AISI 4340 steel (Gust et al. [18]). The high pressure experimental data are not along isotherms and show the temperature increase due to compression. The equation of state provides a reasonable match to the experimental data at compressions below 1.2 which is reasonable for the simulations of interest in this paper. Improved equations of state should be used for overdriven shocks.

3.4 Specific Heat Model for 4340 Steel

The constants for the specific heat model (equation 22) were fit with a least squares technique using experimental data for iron (Wallace et al. [39], Shacklette [35]) and AISI 3040 steel ([19]). The constants used in the simulations are shown in Table 4.

Table 3

Constants used in the Mie-Grüneisen equation of state for 4340 steel.

C_0 (m/s)	S_α	Γ_0
3935	1.578	1.69

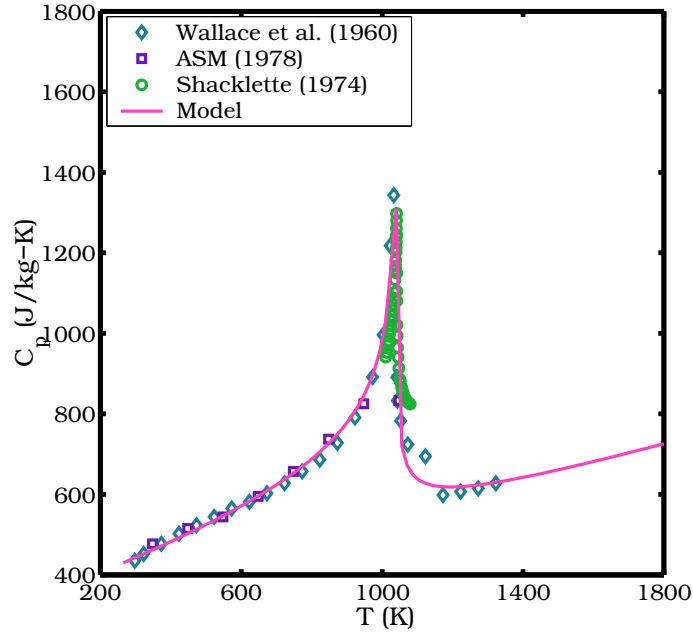


Fig. 4. Comparison of experimental data and model prediction of specific heat for 4340 steel as a function of temperature.

The variation of specific heat with temperature that is predicted by the model is compared to the experimental data in Figure 4. The transition from the bcc α phase to the fcc γ phase is clearly visible in the figure. However, we do not consider such a phase change in the melting temperature model and assume that the iron remains bcc at all pressures.

4 Determination of MTS Model Parameters

The yield strength of high-strength low-alloy (HSLA) steels such as 4340 steel can vary dramatically depending on the heat treatment that it has undergone. This is due to the presence of bcc ferrite-bainite phases along with the dominant bcc martensite phase at room temperature. At higher temperatures (below the α - γ transition) the phases partially transform into the fcc austenite and much of the effect of heat treatment is expected to be lost. Beyond the transition temperature, the alloy is mostly the fcc γ phase that is expected to behave differently from the lower temperature phases. Hence, purely empirical plasticity models require to be recalibrated for

Table 4

Constants used in specific heat model for 4340 steel.

T_c	A_1	B_1	C_1	α	A_2	B_2	C_2	α'
(K)	(J/kg-K)	(J/kg-K)	(J/kg-K)		(J/kg-K)	(J/kg-K)	(J/kg-K)	
1040	190.14	-273.75	418.30	0.20	465.21	267.52	58.16	0.35

different levels of hardness of this material and for different temperatures. In the absence of relevant microstructural models for the various tempers, we assume that there is a direct correlation between the Rockwell C hardness of the alloy steel and the yield stress based on data in the Handbook [19].

The experimental data used to determine the MTS model parameters are from the sources shown in Table 5. All the data are for materials that have been oil quenched after austenitization. More details can be found in the cited references. The 4340 VAR (vacuum arc remelted) steel has a higher fracture toughness than the standard 4340 steel. However, both steels have similar yield behavior (Brown et al. [6]).

The experimental data are either in the form of true stress versus true strain or shear stress versus average shear strain. These curves were digitized manually with care and corrected for distortion. The error in digitization was around 1% on average. The shear stress-strain curves were converted into an effective tensile stress-strain curves by assuming von Mises plasticity as discussed in Goto et al. [14]. The elastic portion of the strain was then subtracted from the total strain assuming a Young's modulus of 213 MPa to get true stress versus plastic strain curves.

The first step in the determination of the parameters for the MTS models is the estimation of the athermal component of the yield stress (σ_a). This parameter is dependent on the Hall-Petch effect and hence on the characteristic martensitic packet size. The packet size will vary for various tempers of steel and will depend on the size of the austenite crystals after the α - γ phase transition. We assume that this constant is independent of the temper and take the value to be 50 MPa based on the value used for HY-100 steel (Goto et al. [14]).

Table 5
Sources of experimental data for 4340 steel.

Material	Rockwell Hardness	Normalize Temp. (C)	Austenitize Temp. (C)	Tempering Temp. (C)	Reference
4340 Steel	C-30				Johnson and Cook [24]
4340 Steel	C-32	900		538	Brown et al. [6]
4340 Steel	C-38	900	870	557	Larson and Nunes [28]
4340 Steel	C-38		850	550	Lee and Yeh [30]
4340 VAR Steel	C-45	900	845	425	Chi et al. [11]
4340 VAR Steel	C-49	900	845	350	Chi et al. [11]

4.1 Determination of σ_i and g_{0i}

From equation (1), it can be seen that σ_i can be found if σ_y and σ_a are known and σ_e is zero. Assuming that σ_e is zero when the plastic strain is zero, and using equation (2), we get the relation

$$\left(\frac{\sigma_y - \sigma_a}{\mu}\right)^{p_i} = \left(\frac{\sigma_i}{\mu_0}\right)^{p_i} \left[1 - \left(\frac{1}{g_{0i}}\right)^{1/q_i} \left[\frac{k_b T}{\mu b^3} \ln\left(\frac{\dot{\epsilon}_{0i}}{\dot{\epsilon}}\right)\right]^{1/q_i}\right] \quad (24)$$

Modified Arrhenius (Fisher) plots based on equation (24) are used to determine the normalized activation energy (g_{0i}) and the intrinsic thermally activated portion of the yield stress (σ_i). We follow the procedure outlined by Goto et al. [14] for HY-100 steel. The parameters used for HY-100 steel ($\dot{\epsilon}_{0i} = 10^{13}/s$, $p_i = 1/2$, $q_i = 3/2$) lead to a good fit to the data at $R_c = 38$. However, the value of the normalized activation energy g_{0i} for $R_c = 30$ is around 40, which is not reasonable. Since the suggested values of p_i should be between 0 and 1 and those for q_i should be between 1 and 2, we have instead used $p_i = 2/3$, $q_i = 1$, and $\dot{\epsilon}_{0i} = 10^8/s$ to generate the Fisher plots. These values lead to reasonably good fits to the experimental data both for the intrinsic and the strain dependent parts of the mechanical threshold stress.

The shear modulus (μ) was calculated using the NP shear modulus model discussed in Sections 2.8 and 3.1. The yield stress at zero plastic strain (σ_y) was computed as the intersection of the stress-plastic strain curve with the stress axis. The value of the Boltzmann constant (k_b) was taken as $1.3806503e-23$ J/K and the magnitude of the Burgers' vector (b) was assumed to be $2.48e-10$ m. The density of the material was assumed to be constant with a value of 7830 kg/m³. Tables 6, 7, and 8 show the intrinsic strengthening component values used to calculate g_{0i} and σ_i .

The straight line fits to the modified Arrhenius data are shown in Figures 5(a), (b), (c), and (d). The spread in the data for R_c 30 (Figure 5(a)) is quite large and may be due to the inclusion of both tension and shear data in the plot. The difference between the yield stress of steels from tension and shear tests at the same strain rate and temperature has been observed both by Johnson and Cook [24] for 4340 steel and by Goto et al. [14] for HY-100. However, this difference is small at low strains and is not expected to affect the intrinsic part of the yield stress much. A more probable cause could be that the range of temperatures and strain rates is quite limited and more data at higher strain rates and temperatures are needed to get a statistically significant correlation.

The Fisher plot data for R_c 32 gives a value of normalized activation energy that is negative. We are unable to determine the cause of this in the absence of sufficient stress-strain data. Numerous choices of σ_a , p_i , q_i , and $\dot{\epsilon}_{0i}$ have been explored in order to achieve a positive value of g_{0i} for the R_c 32 temper. The failure to obtain a positive value of g_{0i} suggests that either the data presented in Brown et al. [6]

are inaccurate or that the R_c 32 temper has some special characteristics that are not accounted for by the MTS model. We have chosen not to use the data for this temper of 4340 steel in the determination of the MTS parameters. However, we do compare the experimental data with our model predictions based on the other tempers of 4340 steel.

Figure 5(b) shows the fit to the Fisher plot data for 4340 steel of hardness R_c 38. The fit can be improved if the values suggested for HY-100 steel are used. The low strain rate data from Larson and Nunes [28] are the outliers near the top of the plot. The hardness of this steel was estimated from tables given in [19] based on the heat treatment and could be higher than R_c 38. However, the Larson and Nunes [28] data are close to the data from Lee and Yeh [30] as can be seen from the plot. A close examination of the high temperature data shows that there is a slight effect due to the α to γ phase transformation at high temperatures.

The stress-strain data for 4340 steel R_c 45 shows anomalous temperature dependent behavior under quasistatic loading, i.e., the yield stress at 373 K is higher than that at 298 K. The fit to the Fisher plot data for this temper of steel is shown in Figure 5(c). The fit to the data can be improved if the value of σ_a is assumed to be 150 MPa and q_i is assumed to be equal to 2. However, larger values of σ_a can lead to large negative values of σ_e at small strains - which is unphysical. The fit to the data for the R_c 49 temper is shown in Figure 5(d). The fit is reasonably good but

Table 6

Fisher plot data used to calculate g_{0i} and σ_i for 4340 steel of hardness R_c 30 and R_c 32.

$[k_b T / \mu b^3 \ln(\dot{\epsilon}_{0i} / \dot{\epsilon})]^{1/q_i}$	$[(\sigma_y - \sigma_a) / \mu]^{p_i}$	T (K)	$\dot{\epsilon}$ (/s)	σ_y (MPa)	μ (GPa)
$R_c = 30$					
0.08333	0.044658	298	0.002	802.577	79.745
0.0782424	0.0432816	298	0.009	768.052	79.745
0.0700974	0.0425718	298	0.1	750.461	79.745
0.0619864	0.0469729	298	1.1	861.843	79.745
0.0408444	0.0447093	298	570	803.874	79.745
0.0747152	0.0435192	500	604	710.861	72.793
0.122804	0.044074	735	650	648.71	64.706
$R_c = 32$					
0.08333	0.0465053	298	0.002	849.751	79.745
0.124676	0.0462771	422	0.002	801.391	75.477
0.188357	0.0476432	589	0.002	775.139	69.730
0.211691	0.0478448	644	0.002	759.94	67.837

Table 7

Fisher plot data used to calculate g_{0i} and σ_i for 4340 steel of hardness R_c 38.

$[k_b T / \mu b^3 \ln(\dot{\epsilon}_{0i} / \dot{\epsilon})]^{1/q_i}$	$[(\sigma_y - \sigma_a) / \mu]^{p_i}$	T (K)	$\dot{\epsilon}$ (/s)	σ_y (MPa)	μ (GPa)
$R_c = 38$					
0.0775492	0.0563156	258	0.0002	1134.12	81.121
0.0911186	0.0542514	298	0.0002	1057.67	79.745
0.0412876	0.0565499	298	500	1122.38	79.745
0.0375715	0.0576617	298	1500	1154.16	79.745
0.117866	0.0551309	373	0.0002	1048.86	77.164
0.0900788	0.0508976	573	500	857.017	70.281
0.0819713	0.0531021	573	1500	910.012	70.281
0.134713	0.0420956	773	500	597.559	63.398
0.11695	0.0461642	773	2500	678.83	63.398
0.173098	0.0367619	973	1500	448.348	56.515
0.165137	0.037095	973	2500	453.773	56.515
0.237617	0.0263176	1173	1500	261.902	49.632
0.226689	0.0287519	1173	2500	291.972	49.632
0.322911	0.0199969	1373	1500	170.886	42.75
0.30806	0.0220299	1373	2500	189.782	42.75

could definitely do with more high strain rate and high temperature data.

The values of σ_i and g_{0i} for the four tempers of 4340 are shown in Table 9. The value of g_{0i} for the R_c 38 temper is quite low and leads to values of the Arrhenius factor (S_i) that are zero beyond temperatures of 800 K. In the following section, we consider the effect of dividing the R_c 38 data into high and low temperature regions.

4.1.1 High temperature effects on σ_i and g_{0i}

More data at higher temperatures and high strain rates are required for better characterization of the R_c 30, R_c 45, and R_c 49 tempers of 4340 steel. In the absence of high temperature data, we can use data for the R_c 38 temper at high temperatures to obtain the estimates of σ_i and g_{0i} . To determine what these high temperature parameters should be, we divide the R_c 38 data into low temperature and high temperature parts. We assume that at temperatures of 573 K and above, all tempers of 4340 steel behave alike. We also assume that changes occur in the intrinsic part of the yield stress and the normalized activation energy beyond the phase transition

Table 8

Fisher plot data used to calculate g_{0i} and σ_i for 4340 steel of hardness R_c 45 and R_c 49.

$[k_b T / \mu b^3 \ln(\dot{\epsilon}_{0i} / \dot{\epsilon})]^{1/q_i}$	$[(\sigma_y - \sigma_a) / \mu]^{p_i}$	T (K)	$\dot{\epsilon}$ (/s)	σ_y (MPa)	μ (GPa)
$R_c = 45$					
0.0514817	0.0645752	173	0.0001	1429.17	84.046
0.0214507	0.0679395	173	1000	1538.34	84.046
0.0934632	0.0611362	298	0.0001	1255.45	79.745
0.038943	0.0683132	298	1000	1473.83	79.745
0.120899	0.062664	373	0.0001	1260.43	77.164
0.0503745	0.0653759	373	1000	1339.85	77.164
$R_c = 49$					
0.0514817	0.0682425	173	0.0001	1548.31	84.046
0.0214507	0.0711498	173	1000	1645.07	84.046
0.0934632	0.0674349	298	0.0001	1446.46	79.745
0.038943	0.0710307	298	1000	1559.63	79.745
0.120899	0.0653628	373	0.0001	1339.46	77.164
0.0503745	0.0694326	373	1000	1461.75	77.164

temperature of iron (1040 K). The resulting low and high temperature Fisher plots for R_c 38 4340 steel are shown in Figures 6 (a) and (b).

A comparison of Figures 5(b) and 6(a) shows that the low temperature Fisher plot has a distinctly lower slope than the plot that contains all the R_c 38 data. The high temperature plot (Figure 6(b)) shows that the slope of the Fisher plot changes slightly after the α to γ phase transition. The values of σ_i and g_{0i} for temperatures between 573 K and 1040 K are 1577.2 MPa and 0.371, respectively. After the phase transition at 1040 K, these quantities take values of 896.1 MPa and 0.576, respectively.

The modified plots of the hardness dependent values of σ_i and g_{0i} close to room

Table 9

Values of σ_i and g_{0i} for four tempers of 4340 steel.

Hardness (R_c)	σ_i (MPa)	g_{0i}
30	867.6	3.31
38	1474.1	0.44
45	1636.6	1.05
49	1752	1.26

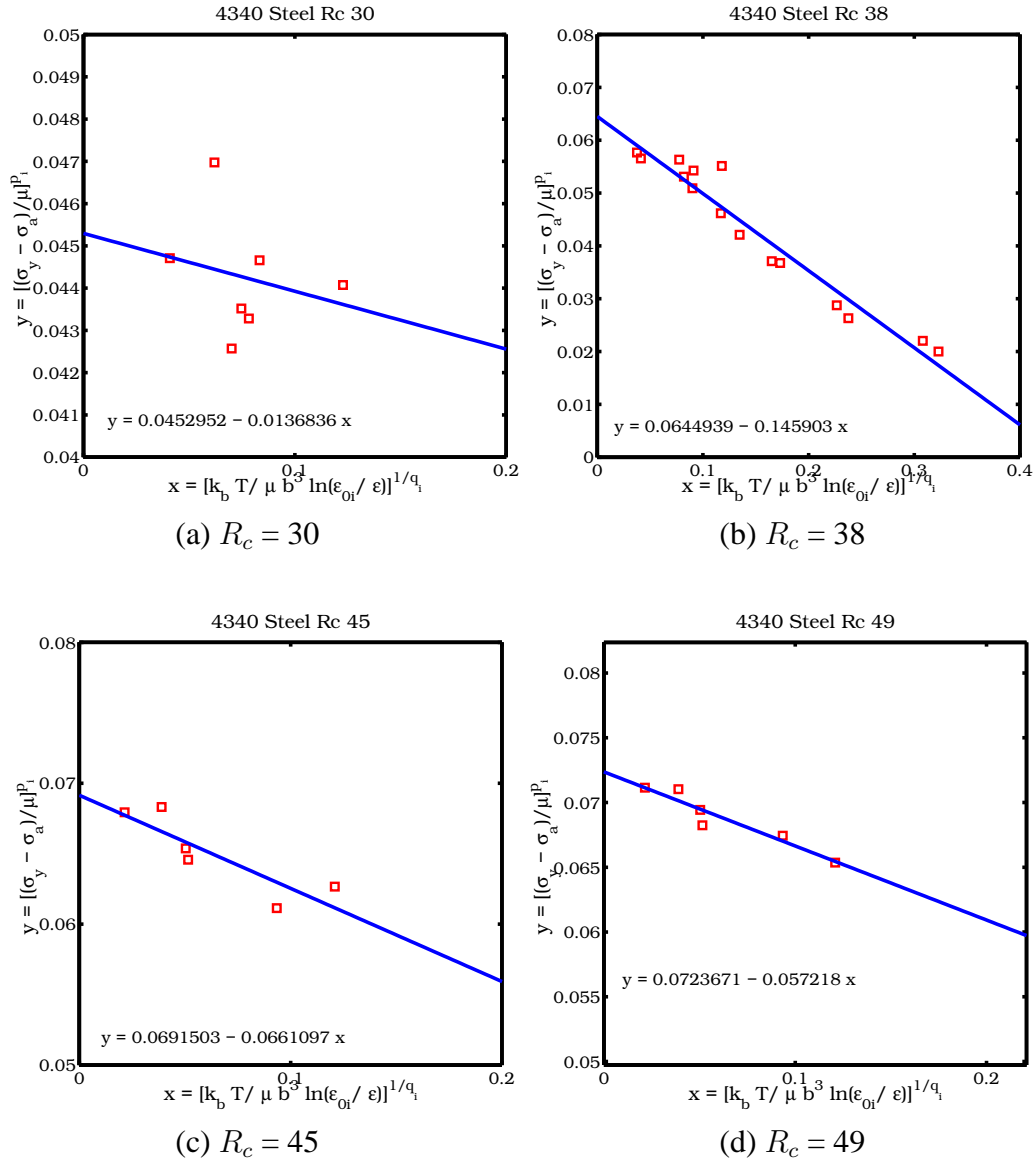


Fig. 5. Fisher plots for the intrinsic component of the MTS model for various tempers of 4340 steel.

temperature are shown in Figure 7. The parameters for the R_c 38 temper of 4340 steel change to $\sigma_i = 1266.3$ MPa and $g_{0i} = 1.85$ if only relatively low temperature data are considered. This value of g_{0i} leads to reasonable values of S_i at high temperatures but the fit to the experimental stress-strain data for the R_c 38 temper becomes poor if these values are used.

An alternative is to use all the R_c 38 data lower than 1040 K to determine the α phase parameters for this temper and to use the data above 1040 K for the γ phase parameters for all tempers. The result of fitting straight lines to the Fisher plot data for R_c 38 is shown in Figure 8. The fits show a jump in value at 1040 K that is not ideal for Newton iterations in a typical elastic-plastic numerical code. However, this jump is more physical than continuous curves that are different for different

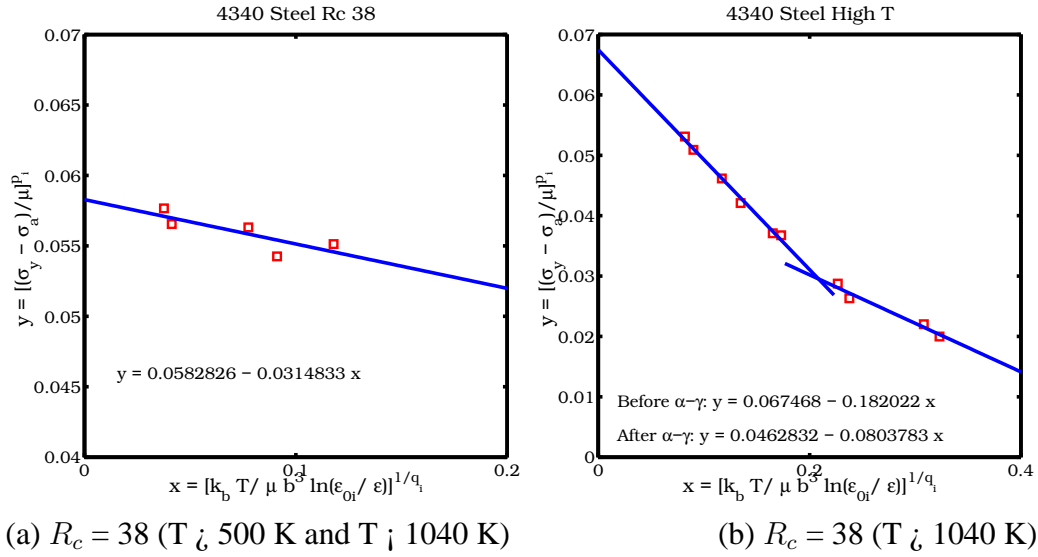


Fig. 6. Fisher plots for the intrinsic component of the MTS model for R_c 38 4340 steel.

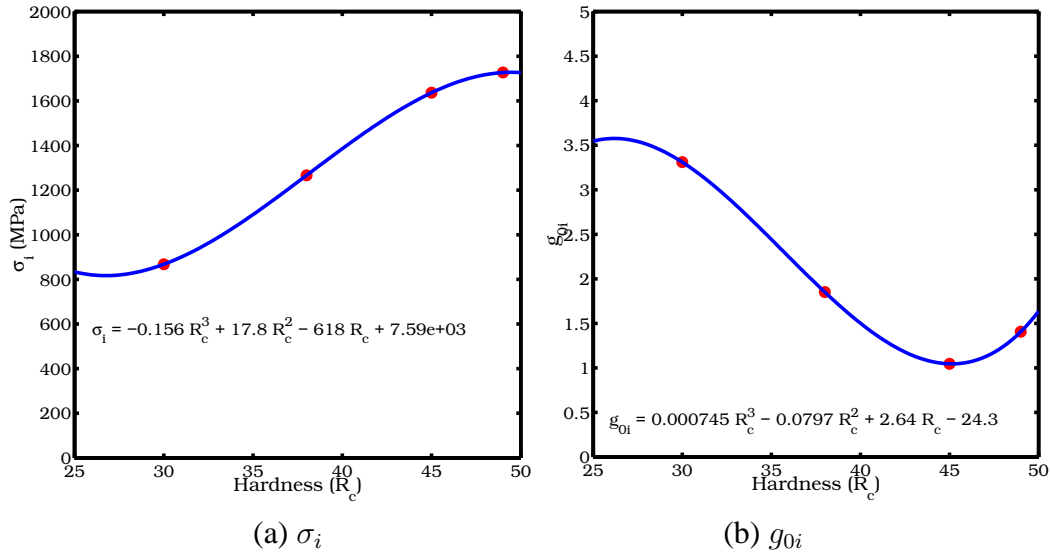


Fig. 7. Values of σ_i and g_{0i} obtained from the Fisher plots for various tempers of 4340 steel close to room temperature.

tempers of 4340 steel. The values of σ_i and g_{0i} for the R_c 38 temper (in the alpha phase) now are 1528 MPa and 0.412, respectively. The value of g_{0i} is again very low and may point to an anomaly in the experimental data presented by Lee and Yeh [30].

Straight line fits to the σ_i and g_{0i} versus R_c data can be used to estimate these parameters for intermediate tempers of the α phase of 4340 steel. These fits are shown in Figure 9. The fit for g_{0i} excludes the anomalous value for R_c 38 4340 steel.

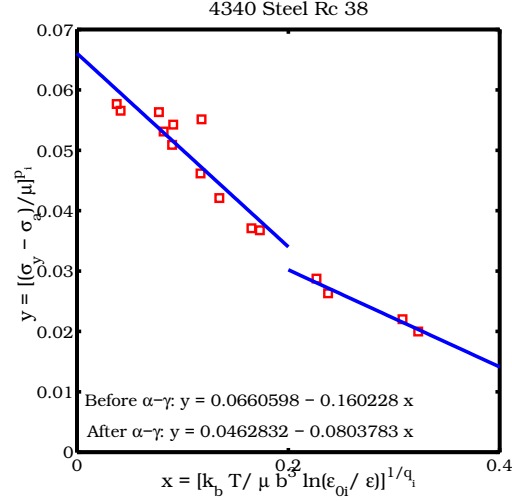


Fig. 8. Fisher plots for the intrinsic component of the MTS model for the α and γ phases of R_c 38 4340 steel.

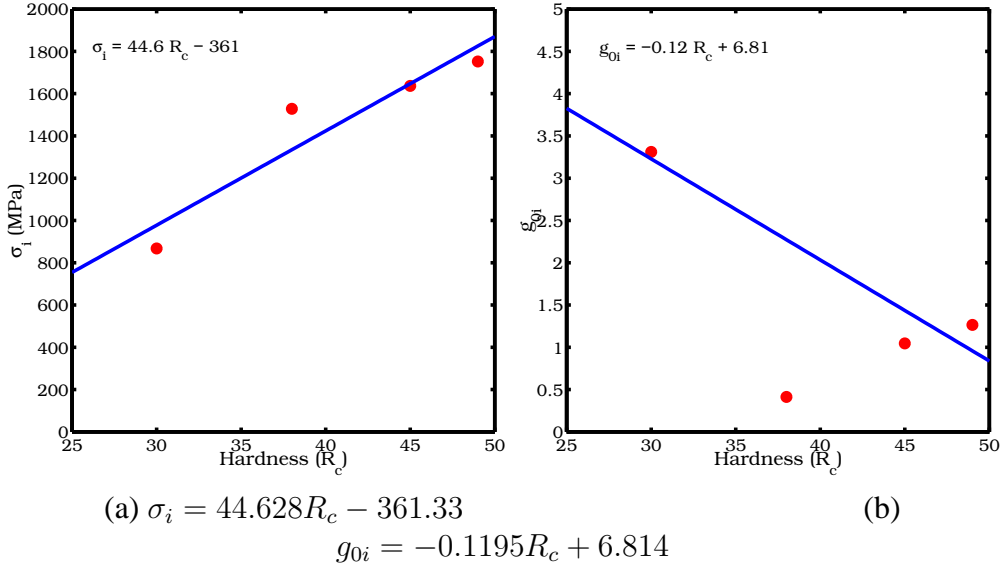


Fig. 9. Values of σ_i and g_{0i} obtained from the Fisher plots for various tempers of the α phase of 4340 steel.

4.2 Determination of σ_{0es} and g_{0es}

Once estimates have been obtained for σ_i and g_{0i} , the value of $S_i\sigma_i$ can be calculated for a particular strain rate and temperature. From equation (1), we then get

$$\sigma_e = \frac{1}{S_e} \left[\frac{\mu_0}{\mu} (\sigma_y - \sigma_a) - S_i\sigma_i \right] \quad (25)$$

which can be used to determine the value of the saturation value (σ_{es}) of the structural evolution stress (σ_e). Given a value of σ_{es} , equation (9) can be used to compute

Table 10

Fisher plot data used to calculate g_{0es} and σ_{es0} for 4340 steel of hardness R_c 30.

$[k_b T / \mu b^3 \ln(\dot{\epsilon}_{es0} / \dot{\epsilon})]$	$\ln(\sigma_{es})$	T_0 (K)	T_s (K)	$\dot{\epsilon}$ (/s)	σ_{es} (MPa)	μ (GPa)
$R_c = 30$						
0.075541	20.986	298	298	0.002	1300	79.745
0.070454	19.807	298	298	0.009	400	79.745
0.062309	19.989	298	298	0.1	480	79.745
0.054198	19.968	298	298	1.1	470	79.745
0.038728	20.986	298	344	570	1300	78.571
0.064987	20.125	500	532	604	550	71.984
0.10315	19.807	735	758	650	400	64.126

σ_{0es} and the corresponding normalized activation energy (g_{0es}) from the relation

$$\ln(\sigma_{es}) = \ln(\sigma_{0es}) - \frac{k_b T}{g_{0es} b^3 \mu} \ln \left(\frac{\dot{\epsilon}}{\dot{\epsilon}_{0es}} \right). \quad (26)$$

The value of σ_{es} can be determined either from a plot of σ_e versus the plastic strain or from a plot of the tangent modulus $\theta(\sigma_e)$ versus σ_e . The value of S_e is required a-priori before σ_e can be calculated. Following Goto et al. [14], we assume that $\dot{\epsilon}_{0e}$, $\dot{\epsilon}_{0es}$, p_e , q_e , and g_{0e} take the values 10^7 /s, 10^7 /s, 2/3, 1, and 1.6, respectively. These values are used to calculate S_e at various temperatures and strain rates. The values of σ_i and g_{0i} used to compute σ_e vary with hardness for temperatures below 573 K, and are constant above that temperature as discussed in the previous section. Adiabatic heating is assumed at strain rates above 500 /s.

Representative plots of σ_e versus the plastic strain is shown in Figure 10(a) and the corresponding θ versus σ_e plot is shown in Figure 10(b) for the R_c 38 temper at a strain rate of 1500 /s. Similar plots for the R_c 49 temper at a strain rate of 0.0001 /s are shown in Figures 10(c) and (d). Errors in the fitting of σ_i and g_{0i} can cause the computed value of σ_e to be above or below zero at zero plastic strain. The plotted value of the tangent modulus is the mean of the tangent moduli at each value of σ_e (except for the first and last points). The saturation stress (σ_{es}) is the value at which σ_e becomes constant or θ is zero.

The data used to compute the parameters σ_{es0} and g_{0es} are shown in Tables 10, 11, 12, and 13. The straight line fit to the data for the R_c 30 temper is shown in Figure 11(a). The fit to the α phase for R_c 38 4340 steel is shown in Figure 11(b). Similar Fisher plots for R_c 45 and R_c 49 4340 steel are shown in Figures 11(c) and (d).

The correlation between the modified Arrhenius relation and the data is quite poor

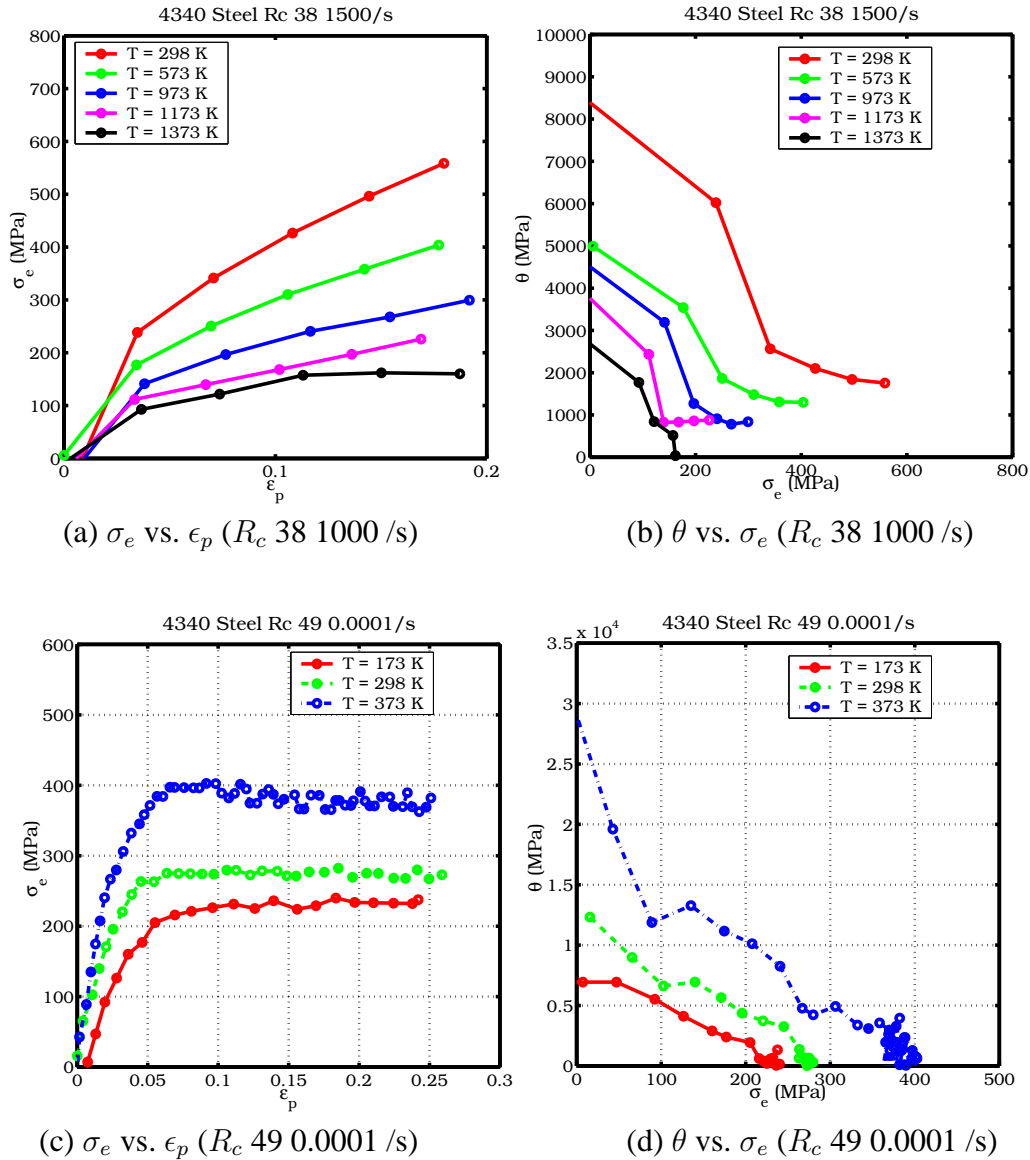


Fig. 10. Plots used to determine the saturation value (σ_{es}) of the structure evolution stress (σ_e).

suggesting that the strain dependent part of the mechanical threshold stress does not follow an Arrhenius relation. However, we do not have information on the standard deviation of the experimental data and therefore cannot be confident about this possibility. We continue to assume, following [14] for HY-100, that a modified Arrhenius type of temperature and strain rate dependence is acceptable for 4340 steel.

Values of σ_{es0} and g_{0es} computed from the fits are shown in Table 14. There is considerable variation among the values of the normalized activation energy and the saturation stress at 0 K between the various temps. For intermediate temps a median value of 0.284 is assumed for g_{0es} and the mean value of 705.5 MPa is assumed for σ_{es0} . Straight line fits to the data, as shown in Figure 12 could also

Table 11

Fisher plot data used to calculate g_{0es} and σ_{es0} for 4340 steel of hardness R_c 38.

$[k_b T / \mu b^3 \ln(\dot{\epsilon}_{es0} / \dot{\epsilon})]$	$\ln(\sigma_{es})$	T_0 (K)	T_s (K)	$\dot{\epsilon}$ (/s)	σ_{es} (MPa)	μ (GPa)
$R_c = 38$						
0.07092	21.129	258	258	0.0002	1500	81.121
0.08333	20.986	298	298	0.0002	1300	79.745
0.10779	21.254	373	373	0.0002	1700	77.164
0.036227	20.212	298	320	500	600	79.183
0.075873	20.05	573	591	500	510	69.826
0.11153	19.552	773	785	500	310	63.096
0.037964	20.618	298	371	1500	900	77.886
0.070669	20.367	573	614	1500	700	69.246
0.14023	20.03	973	988	1500	500	56.154
0.098146	20.125	773	815	2500	550	62.342
0.13342	20.088	973	995	2500	530	55.989
0.19164	19.519	1173	1185	1500	300	49.282
0.25895	18.891	1373	1381	1500	160	42.505
0.18261	19.163	1173	1193	2500	210	49.047
0.24641	19.376	1373	1388	2500	260	42.289

Table 12

Fisher plot data used to calculate g_{0es} and σ_{es0} for 4340 steel of hardness R_c 45.

$[k_b T / \mu b^3 \ln(\dot{\epsilon}_{es0} / \dot{\epsilon})]$	$\ln(\sigma_{es})$	T_0 (K)	T_s (K)	$\dot{\epsilon}$ (/s)	σ_{es} (MPa)	μ (GPa)
$R_c = 45$						
0.047192	19.414	173	173	0.0001	270	84.046
0.085675	17.034	298	298	0.0001	25	79.745
0.11082	19.715	373	373	0.0001	365	77.164
0.021177	19.139	173	211	1000	205	83.067
0.034507	18.683	298	327	1000	130	79.004
0.043234	18.826	373	397	1000	150	76.553

be used to determine the values of g_{0es} and σ_{es0} for intermediate tempers of 4340 steel. The data above 1040 K are assumed to be for the γ phase of 4340 steel. Fits to the data at these high temperatures lead to values of 0.294 and 478.36 MPa for g_{0es} and σ_{es0} , respectively, for the γ phase.

Table 13

Fisher plot data used to calculate g_{0es} and σ_{es0} for 4340 steel of hardness R_c 49.

$[k_b T / \mu b^3 \ln(\dot{\epsilon}_{es0} / \dot{\epsilon})]$	$\ln(\sigma_{es})$	T_0 (K)	T_s (K)	$\dot{\epsilon}$ (/s)	σ_{es} (MPa)	μ (GPa)
$R_c = 49$						
0.047192	19.254	173	173	0.0001	230	84.046
0.085675	19.376	298	298	0.0001	260	79.745
0.11082	19.756	373	373	0.0001	380	77.164
0.02075	18.951	173	207	1000	170	83.17
0.035325	19.45	298	334	1000	280	78.826
0.043234	19.45	373	397	1000	280	76.553

4.3 Determination of hardening rate θ

The modified Voce rule for the hardening rate (θ) (equation (5)) is purely empirical. To determine the temperature and strain rate dependence of θ , we plot the variation of θ versus the normalized structure evolution stress assuming hyperbolic tangent dependence of the rate of hardening on the mechanical threshold stress. We assume that $\alpha = 3$.

Figures 13(a), (b), (c), and (d) show some representative plots of the variation of θ with $F := \tanh(\alpha\sigma_e/\sigma_{es})/\tanh(\alpha)$. As the plots show, the value of θ_1 (the value of θ at $F = 1$) can be assumed to be zero for most of the data.

It is observed from Figure 13(a) that there is a strong strain rate dependence of θ that appears to override the expected decrease with increase in temperature for the R_c 30 temper of 4340 steel. It can also be seen that θ is almost constant at 298 K and 0.002/s strain rate reflecting linear hardening. However, the hyperbolic tangent rule appears to be a good approximation at higher temperatures and strain rates.

The plot for R_c 38 4340 steel (Figure 13(b)) shows a strong temperature dependence of θ with the hardening rate decreasing with increasing temperature. The same behavior is observed for all high strain rate data. However, for the data at a

Table 14

Values of σ_{es0} and g_{0es} for four tempers of 4340 steel.

Hardness (R_c)	σ_{es0} (MPa)	g_{0es}
30	1316.1	0.088
38	1058.4	0.232
45	173.5	0.336
49	274.9	1.245

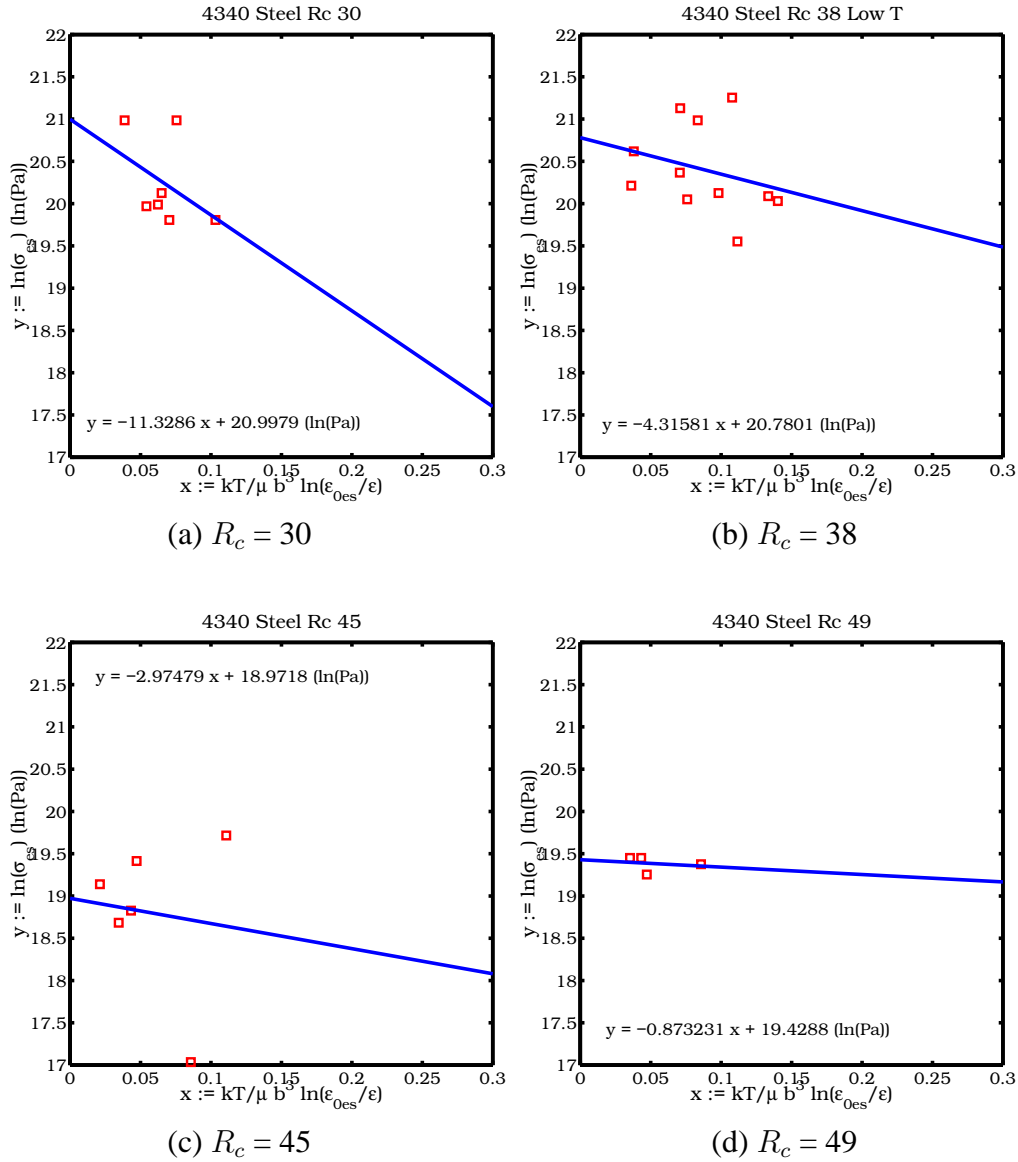


Fig. 11. Fisher plots for the structure evolution dependent component of the MTS model for various tempers of 4340 steel.

strain rate of 0.0002/s, there is an increase in θ with increasing temperature. Figures 13(c) and (d) also show an increase in θ with temperature. These reflect an anomaly in the constitutive behavior of 4340 steel for relatively low temperatures (below 400 K) (Tanimura and Duffy [37]) that cannot be modeled continuously using an Arrhenius law and needs to be characterized in more detail.

Fits to the experimental data of the form shown in equation (6) have been attempted. The resulting values of a_{00} , a_{01} , a_{02} , and a_{03} are plotted as functions of R_c in Figures 14(a), (b), (c), and (d), respectively. The points show the values of the constants for individual tempers while the solid line shows the median value. These figures show that the constants vary considerably and also change sign for different tempers. On average, the strain rate dependence is small for all the tempers but

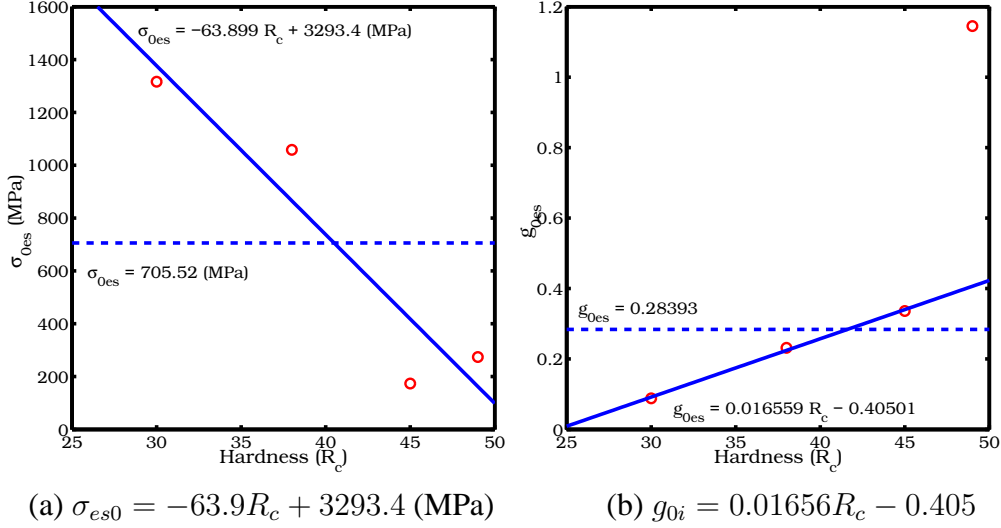


Fig. 12. Values of σ_{es0} and g_{0es} obtained from the Fisher plots for various tempers of the α phase of 4340 steel.

significant. The R_c 30 and R_c 45 data points in Figure 14(d) reflect an increase in hardening rate with temperature that is nonphysical at high temperatures. Instead of using these fits to the experimental data, we have decided to ignore the strain rate dependence of the hardening rate and fit a curve to all the data taking only temperature dependence into account (as shown in Figure 15). Distinctions have not been made between various tempers of 4340 steel to determine this average hardening rate. However, we do divide the data into two parts based on the α - γ phase transition temperature.

The resulting equations for θ_0 as functions of temperature are

$$\theta_0 = \begin{cases} 15719 - 10.495T \text{ (MPa)} & \text{for } T < 1040K \\ 7516 - 3.7796T \text{ (MPa)} & \text{for } T > 1040K \end{cases} \quad (27)$$

This completes the determination of the parameters for the MTS model.

5 Comparison of MTS model predictions and experimental data

The performance of the MTS model for 4340 steel is compared to experimental data in this section. In the figures that follow, the MTS predictions are shown as dotted lines while the experimental data are shown as solid lines with symbols indicating the conditions of the test. Isothermal conditions have been assumed for strain rates less than 500/s and adiabatic heating is assumed to occur at higher strain rates.

Figure 16(a) shows the low strain rate experimental data and the corresponding MTS predictions for the R_c 30 temper of 4340 steel. Comparisons for moderately

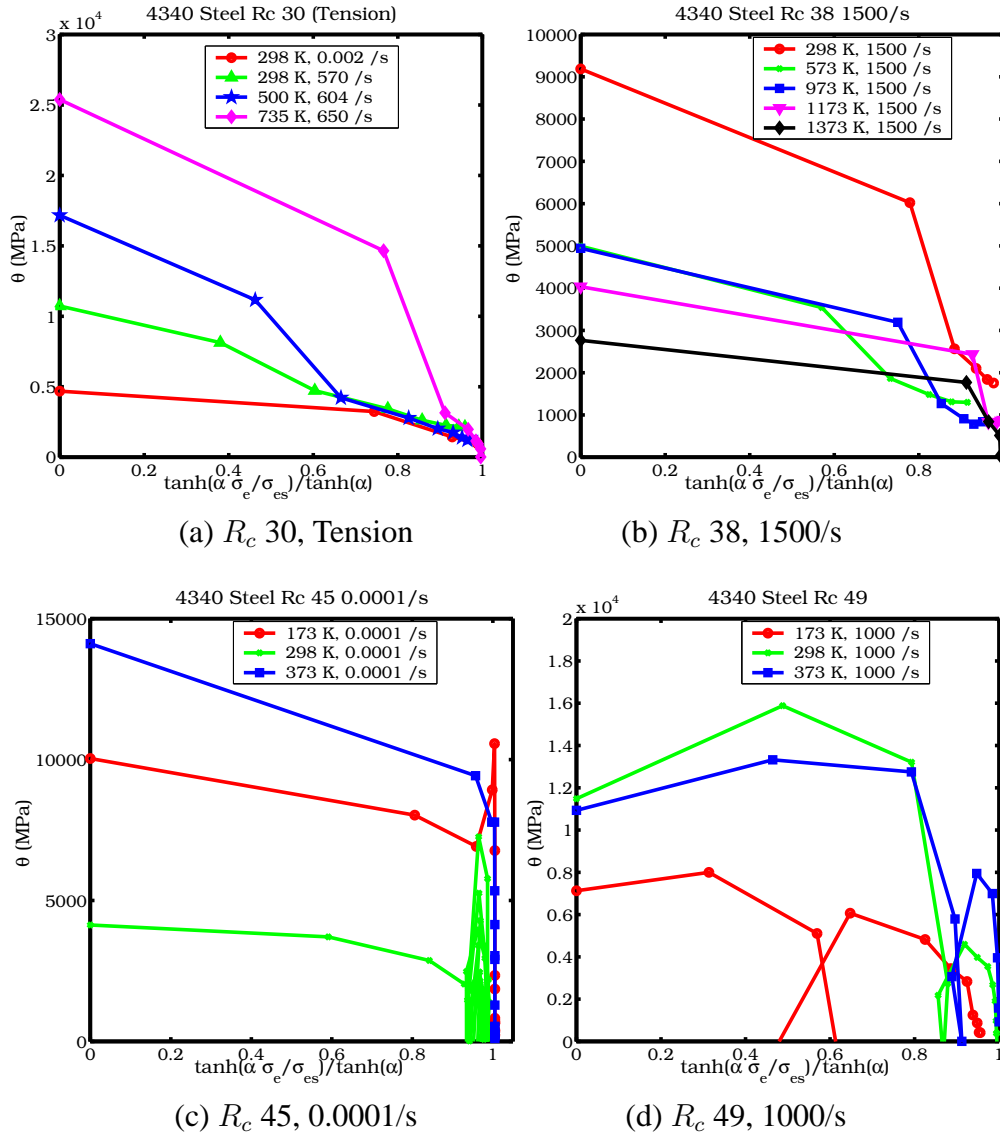


Fig. 13. Plots used to determine θ_0 as a function of temperature and strain rate.

high strain rates and high temperatures for the R_c 30 temper are shown in Figure 16(b). The model matches the experimental curves quite well for low strain rates (keeping in mind the difference between the stress-strain curves in tension and in shear). The high strain rate curves are also accurately reproduced though there is some error in the initial hardening modulus for the 650 /s and 735 K case. This error can be eliminated if the effect of strain rate is included in the expression for θ_0 . The maximum modeling error for this temper is around 15%.

We have not used the R_c 32 experimental data to fit the MTS model parameters. As a check of the appropriateness of the relation between the parameters and the R_c hardness number, we have plotted the MTS predictions versus the experimental data for this temper in Figure 17. Our model predicts a stronger temperature dependence for this temper than the experimental data. However, the initial high

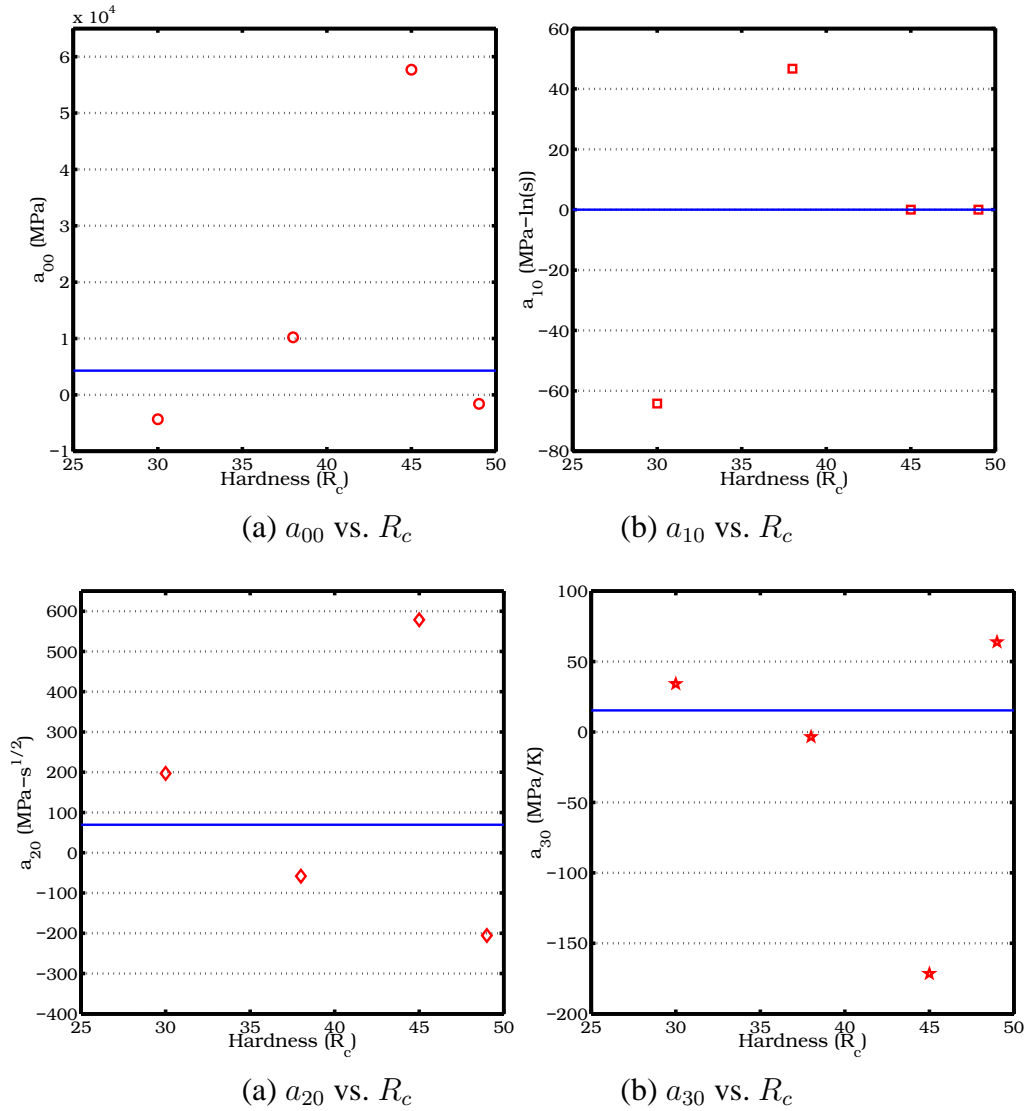


Fig. 14. Variation of the constants fit to the hardening rate equation for various tempers of 4340 steel.

temperature yield stress is reproduced quite accurately while the ultimate tensile stress is reproduced well for the lower temperatures.

The low strain rate stress-strain curves for R_c 38 4340 steel are shown in Figure 18. High strain rate stress-strain curves for the R_c 38 temper are shown in Figures 19(a), (b), and (c). The saturation stress predicted at low strain rates is around 20% smaller than the observed values at large strains. The anomaly at 373 K is not modeled accurately by the MTS parameters used. On the other hand, the high strain rate data are reproduced quite accurately by the MTS model with a modeling error of around 5% for all temperatures.

Experimental data for the R_c 45 temper are compared with MTS predictions in Figures 20 (a) and (b). The MTS model under predicts the low strain rate yield

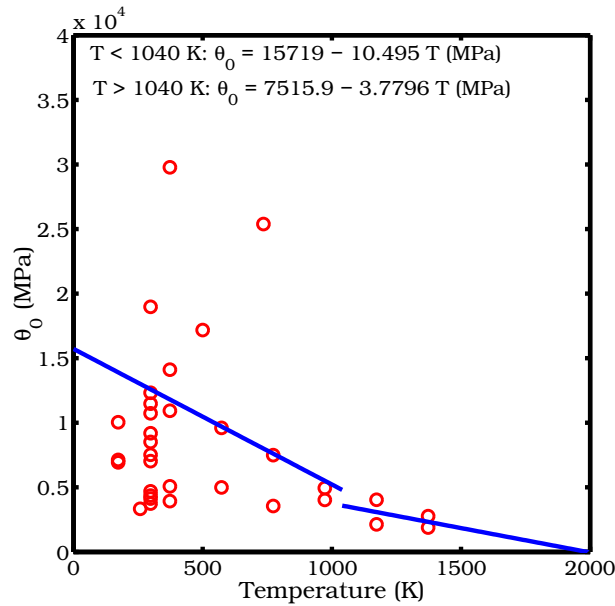


Fig. 15. Variation of θ_0 with temperature.

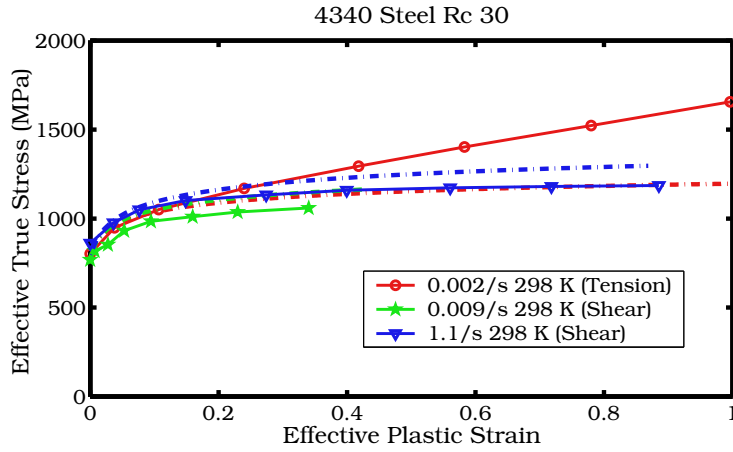
stress and initial hardening modulus by around 15% for both the 173 K and 373 K data. The prediction is within 10% for the 298 K data. The anomaly at 373 K is clearly visible for the low strain rate plots shown in Figure 20(a). The high strain rate data are reproduced quite accurately for all three temperatures and the error is less than 10%.

Comparisons for the R_c 49 temper are shown in Figures 21 (a) and (b). The model predicts the experimental data quite accurately for 173 K and 298 K at a strain rate of 0.0001/s. However, the anomalous behavior at 373K is not predicted and a modeling error of around 15% is observed for this temperature. For the high strain rate cases shown in Figure 21(b), the initial hardening modulus is under-predicted and saturation is predicted at a lower stress than observed. In this case, the modeling error is around 10%.

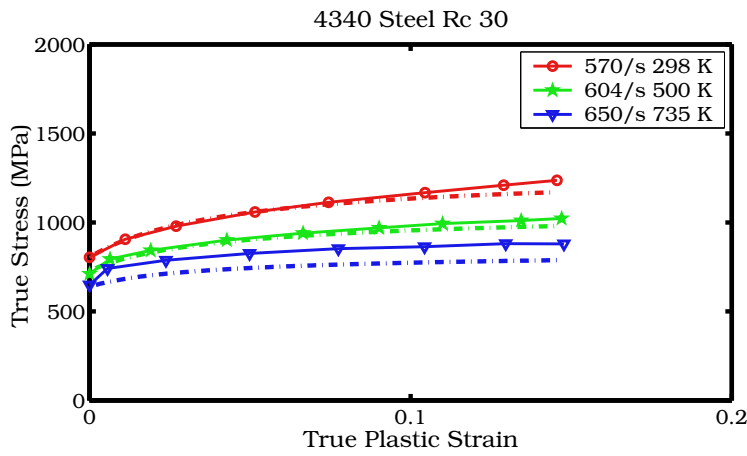
The comparisons of the MTS model predictions with experimental data shows that the predictions are all within an error of 20% for the range of data examined. If we assume that the standard deviation of the experimental data is around 5% (Hanson [20]) then the maximum modeling error is around 15% with around a 5% mean. This error is quite acceptable for numerical simulations, provided the simulations are conducted within the range of conditions used to fit the data.

6 MTS model predictions over an extended range of conditions

In this section, we compare the yield stresses predicted for a R_c 40 temper of 4340 steel by the MTS model with those from the Johnson-Cook (JC) model over a



(a) Low strain rates.



(b) High strain rates.

Fig. 16. Comparison of MTS prediction with experimental data from Johnson and Cook [24] for the R_c 30 temper of 4340 steel.

range of strain rates and temperatures. In the plots shown in this section, the yield stress (σ_y) is the Cauchy stress, the plastic strain (ϵ_p) is the true plastic strain, the temperatures (T) are the initial temperatures and the strain rates $\dot{\epsilon}$ are the nominal strain rates. The effect of pressure on the density and melting temperature has been ignored in the MTS calculations discussed in this section.

6.1 Parameters for the Johnson-Cook model

The value of σ_0 for 4340 steel in the Johnson-Cook model varies with the temper of the steel. We have fit the yield stress versus R_c hardness curve for 4340 steel from the ASM handbook [19] to determine the value of σ_0 for various tempers. The equation for the fit is

$$\sigma_0 = \exp(A_1 R_c + A_2) \text{ (MPa)} \quad (28)$$

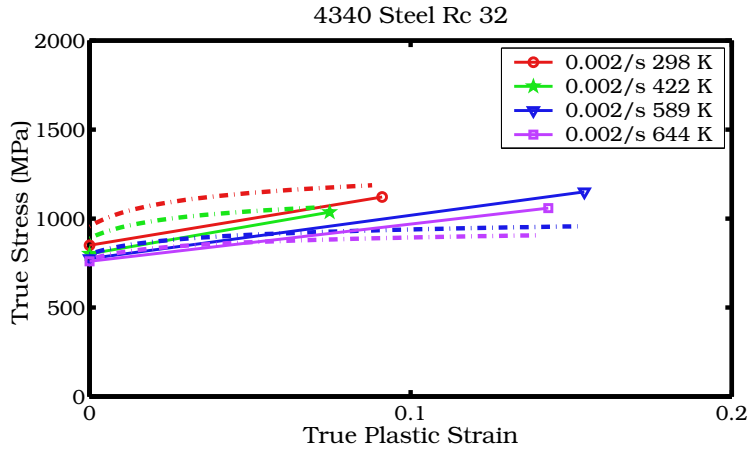


Fig. 17. Comparison of MTS prediction with experimental data from Brown et al. [6] for the R_c 32 temper of 4340 steel.

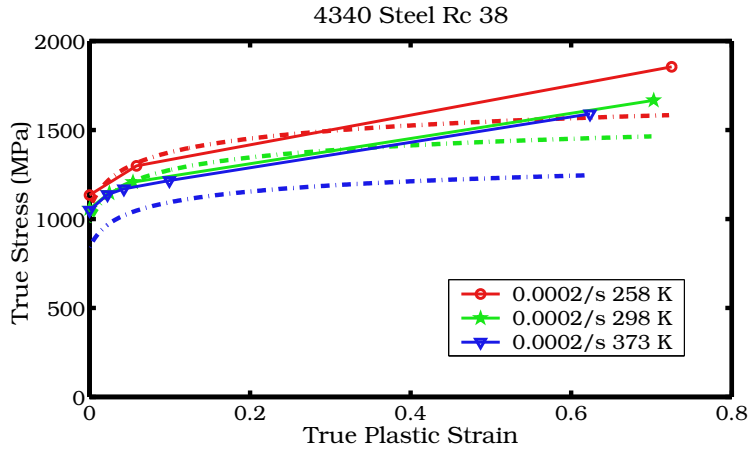
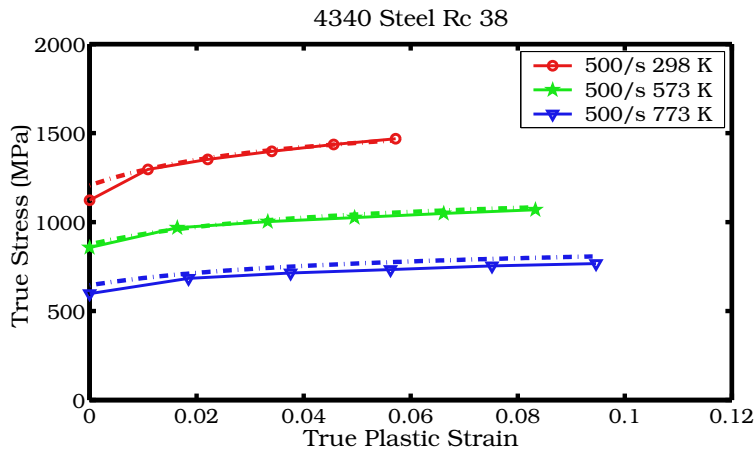
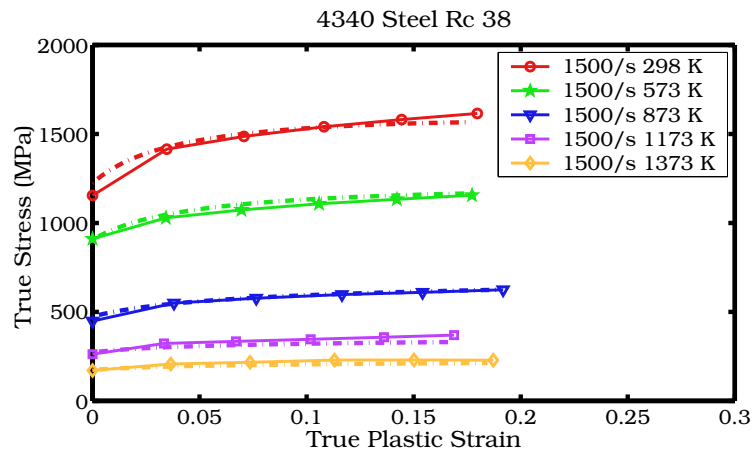


Fig. 18. Comparison of MTS prediction with experimental data from Larson and Nunes [28] for the R_c 38 temper of 4340 steel at 0.0002/s strain rate.

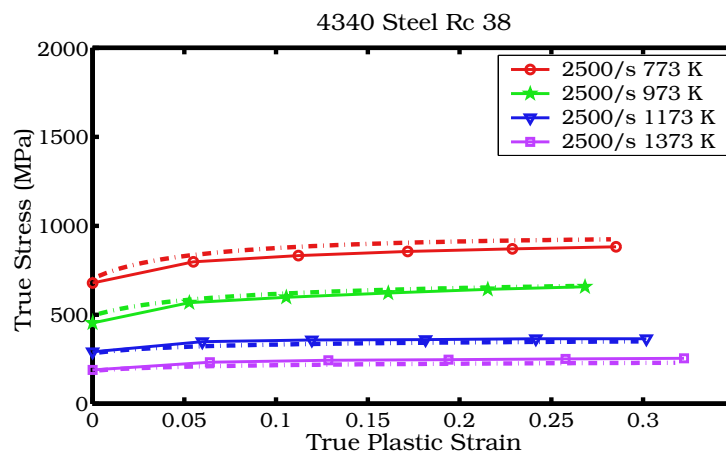
where $A_1 = 0.0355 \ln(\text{MPa})$, $A_2 = 5.5312 \ln(\text{MPa})$, and R_c is the Rockwell-C hardness of the steel. The value of $B/\sigma_0 = 0.6339$ is assumed to be a constant for all tempers. The strain hardening exponent (n) is 0.26 and the strain rate dependence parameter (C) is 0.014, for all tempers. The reference strain rate $\dot{\epsilon}_0$ is 1 /s. For temperatures less than 298 K, thermal softening is assumed to be linear and the parameter m takes a value of 1. Above 298 K and lower than 1040 K, m is assumed to be 1.03, and beyond 1040 K, m is taken as 0.5 (Lee and Yeh [30]). The reference temperature (T_r) is 298 K and the melt temperature (T_m) is kept fixed at 1793 K. These parameters provide a reasonable fit to the experimental data presented earlier in the context of the MTS model.



(a) Strain Rate = 500 /s

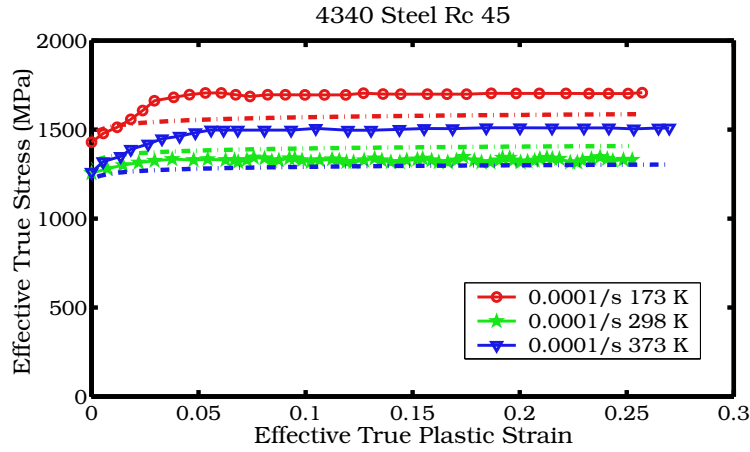


(b) Strain Rate = 1500 /s

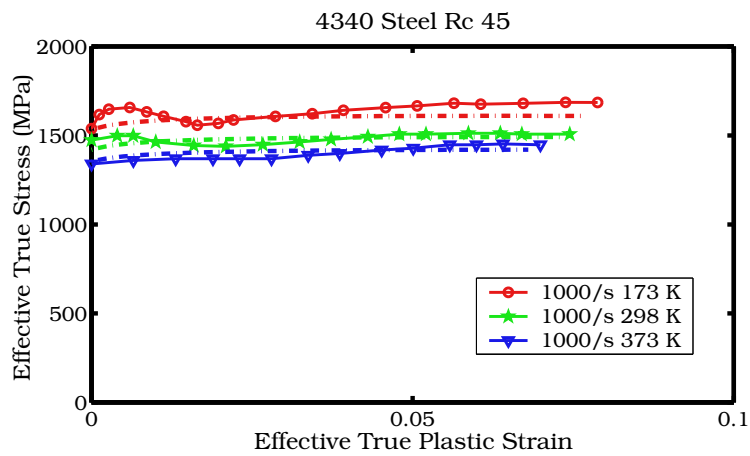


(c) Strain Rate = 2500 /s

Fig. 19. Comparison of MTS prediction with experimental data from Lee and Yeh [30] for the R_c 38 temper of 4340 steel at high strain rates.



(a) Strain Rate = 0.0001 /s



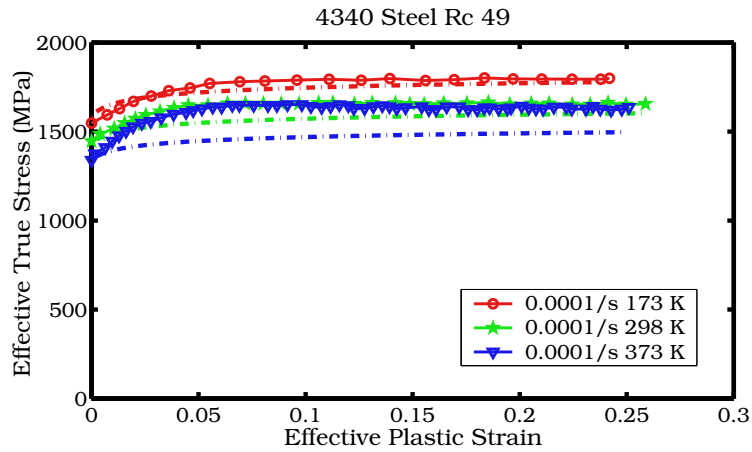
(b) Strain Rate = 1000 /s

Fig. 20. Comparison of MTS prediction with experimental data from Chi et al. [11] for the R_c 45 temper of 4340 steel.

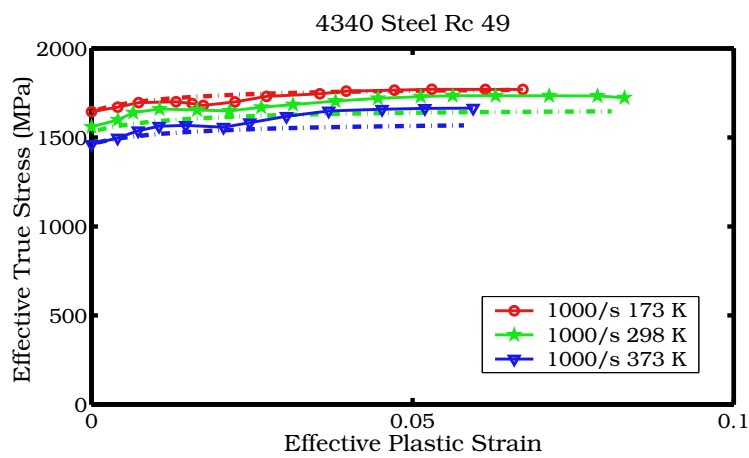
6.2 Yield stress versus plastic strain

Figures 22(a) and (b) show the yield stress-plastic strain curves predicted by the MTS and JC models, respectively. The initial temperature is 600 K and adiabatic heating is assumed for strain rates above 500 /s. The strain rate dependence of the yield stress is less pronounced for the MTS model than for the JC model. The hardening rate is higher at low strain rates for the JC model. The rapid increase in the strain-rate dependence of the yield stress at strain rates above 1000 /s (Nicholas [33]) is not predicted by either model and is probably due to the limited high rate data used to fit the models.

The temperature dependence of the yield stress for a strain rate of 1000 /s is shown in Figures 23(a) and (b). Both models predict similar stress-strain responses as a function of temperature. However, the initial yield stress is higher for the MTS model and the initial hardening rate is lower than that predicted by the JC model for



(a) Strain Rate = 0.0001 /s



(b) Strain Rate = 1000 /s

Fig. 21. Comparison of MTS prediction with experimental data from Chi et al. [11] for the R_c 49 temper of 4340 steel.

initial temperatures of 300K and 700 K. For the high temperature data, the MTS model predicts lower yield stresses.

6.3 Yield stress versus strain rate

The strain rate dependence of the yield stress (at a temperature of 600 K) predicted by the MTS and JC models is shown in Figures 24(a) and (b), respectively. The JC model shows a higher amount of strain hardening than the MTS model. The strain rate hardening of the MTS model appears to be closer to experimental observations (Nicholas [33]) than the JC model.

The temperature and strain rate dependence of the yield stress at a plastic strain of 0.3 is shown in Figures 25(a) and (b). Above the phase transition temperature, the MTS model predicts more strain rate hardening than the JC model. However, at

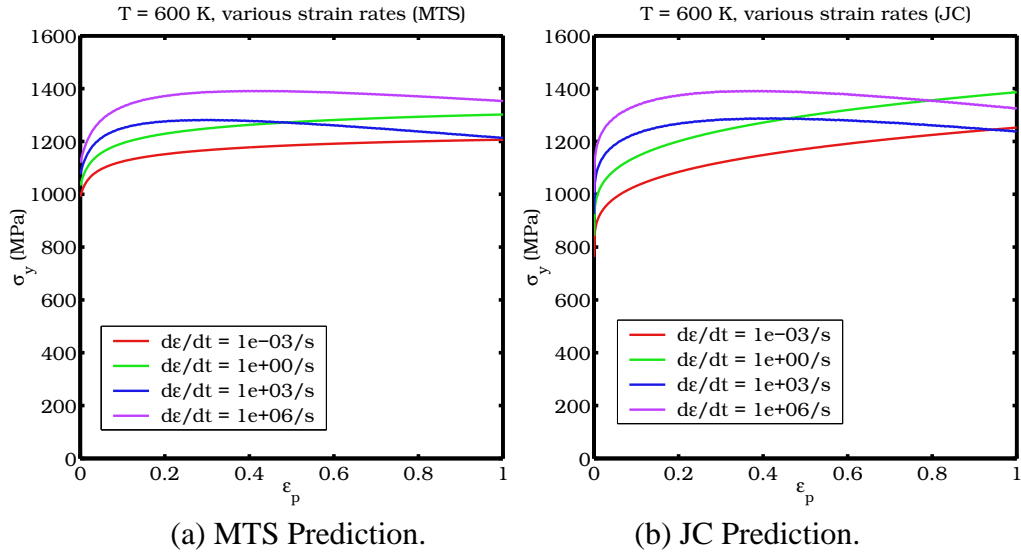


Fig. 22. Comparison of MTS and JC predictions of yield stress versus plastic strain at various strain rates for $T_0 = 600$ K.

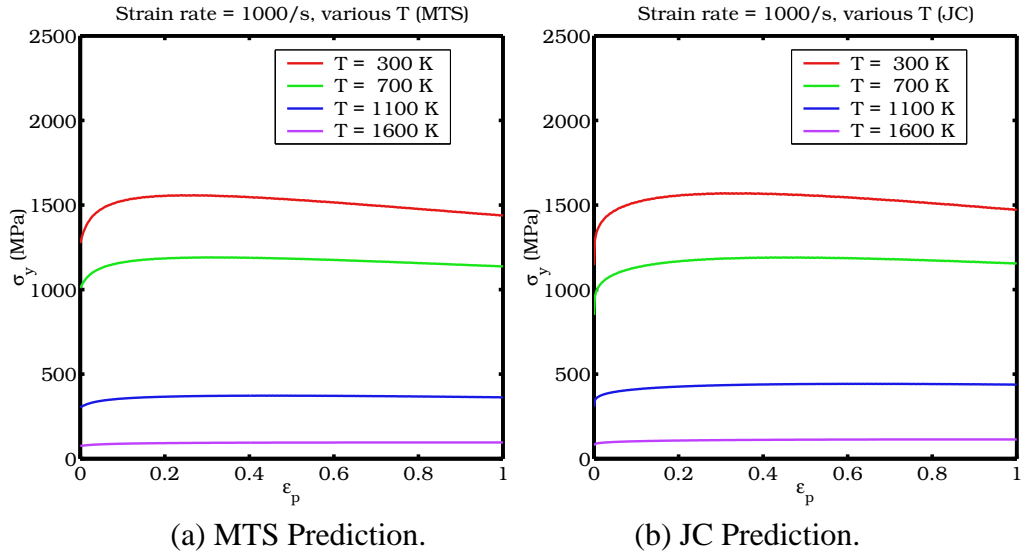


Fig. 23. Comparison of MTS and JC predictions of yield stress versus plastic strain at various strain rates for $\dot{\epsilon} = 1000$ /s.

700 K, both models predict quite similar yield stresses. At room temperature, the JC model predicts a higher rate of strain rate hardening than the MTS model and is qualitatively closer to experimental observations.

6.4 Yield stress versus temperature

The temperature dependence of the yield stress for various plastic strains (at a strain rate of 1000 /s) is shown in Figures 26(a) and (b). The sharp change in the value of

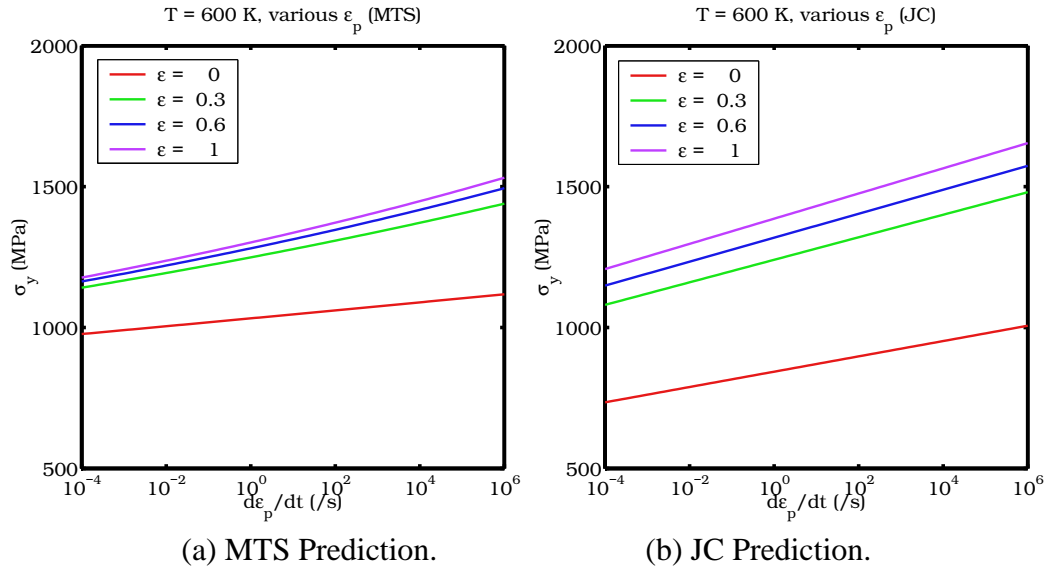


Fig. 24. Comparison of MTS and JC predictions of yield stress versus strain rate at various plastic strains for $T_0 = 600$ K.

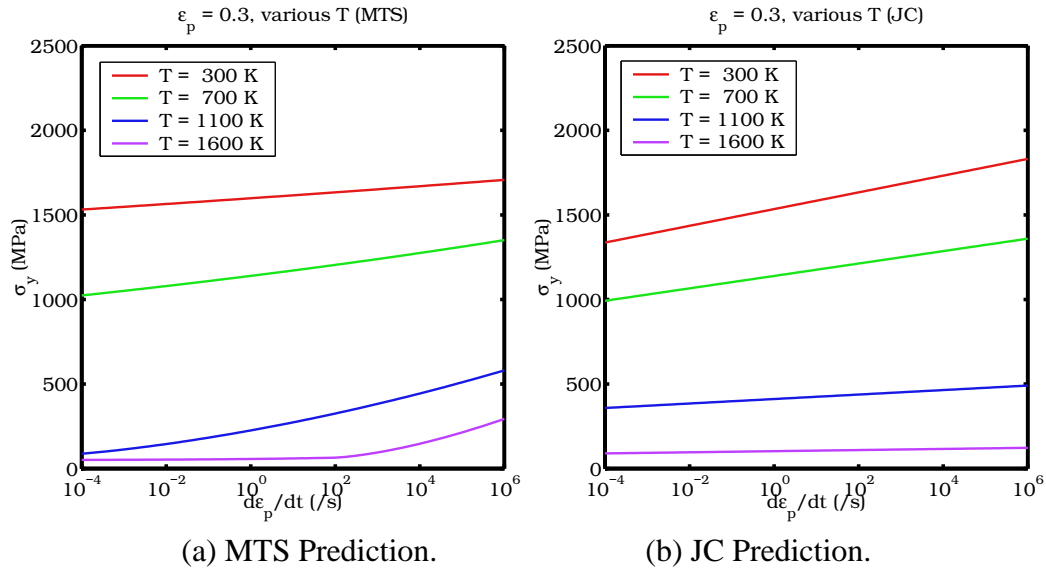


Fig. 25. Comparison of MTS and JC predictions of yield stress versus strain rate at various temperatures for $\epsilon_p = 0.3$.

the yield stress at the phase transition temperature may be problematic for Newton methods used in the determination of the plastic strain rate. We suggest that at temperatures close to the phase transition temperature, the high temperature parameters should be used in numerical computations. The figures show that both the models predict similar rates of temperature dependence of the yield stress.

The temperature dependence of the yield stress for various strain rates (at a plastic strain of 0.3) is shown in Figures 27(a) and (b). In this case, the MTS model predicts at smaller strain rate effect at low temperatures than the JC model. The strain

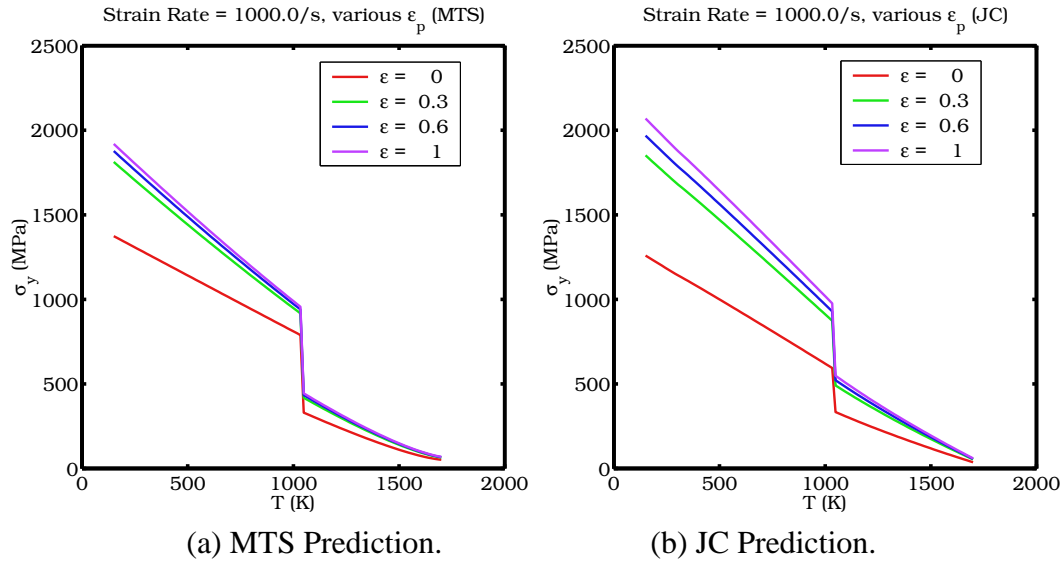


Fig. 26. Comparison of MTS and JC predictions of yield stress versus temperature at various plastic strains for $\dot{\epsilon} = 1000/s$.

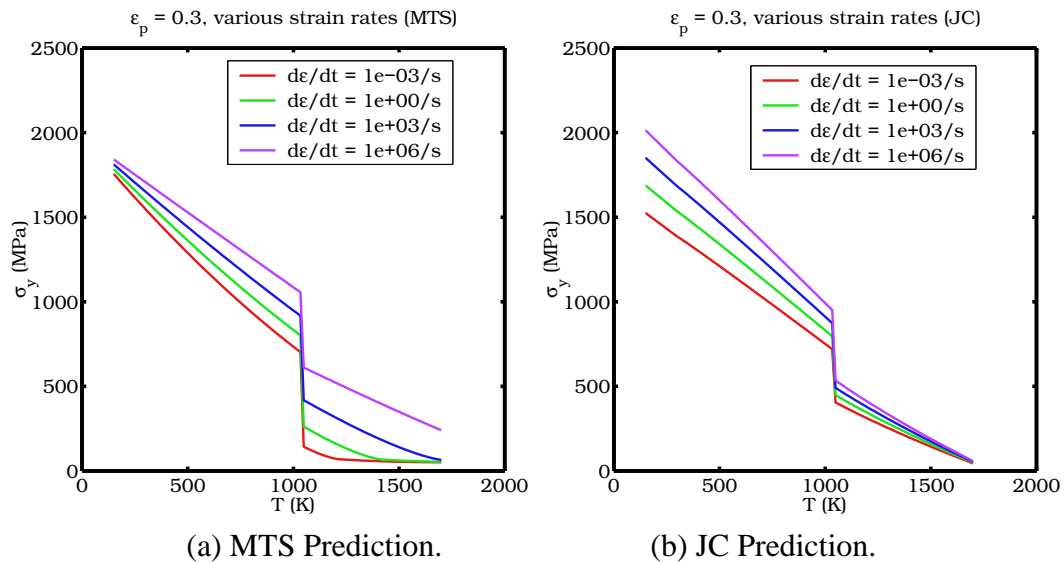


Fig. 27. Comparison of MTS and JC predictions of yield stress versus temperature at various strain rates for $\epsilon_p = 0.3$.

rate dependence of the yield stress increases with temperature for the MTS model while it decreases with temperature for the JC model. The JC model appears to predict a more realistic behavior because the thermal activation energy for dislocation motion is quite low at high temperatures. However, the MTS model fits high temperature/high strain rate experimental data better than the JC model and we might be observing the correct behavior in the MTS model.

6.5 Taylor impact tests

For further confirmation of the effectiveness of the MTS model, we have simulated three-dimensional Taylor impact tests using the Uintah code (Banerjee [2]). Details of the code, the algorithm used, and the validation process have been discussed elsewhere (Banerjee [2, 3]).

It is well known that the final length of a Taylor impact cylinder scales with the initial velocity. Figure 28 shows some experimental data on the final length of cylindrical Taylor impact specimens as a function of initial velocity. We are interested in temperatures higher than room temperature. For clarity, we have separated the high temperature tests from the room temperature tests by adding an initial internal energy component to the initial kinetic energy density. We have simulated three Taylor tests at three energy levels (marked with crosses on the plot).

The four cases that we have simulated have the following initial conditions:

- (1) **Case 1:** $R_c = 30$; $L_0 = 25.4$ mm; $D_0 = 7.62$ mm; $U_0 = 208$ m/s; $T_0 = 298$ K; Source Johnson and Cook [23].
- (2) **Case 2:** $R_c = 40$; $L_0 = 30.0$ mm; $D_0 = 6.0$ mm; $U_0 = 312$ m/s; $T_0 = 725$ K; Source Gust [17].
- (3) **Case 3:** $R_c = 40$; $L_0 = 30.0$ mm; $D_0 = 6.0$ mm; $U_0 = 160$ m/s; $T_0 = 1285$ K; Source Gust [17].
- (4) **Case 4:** $R_c = 40$; $L_0 = 30.0$ mm; $D_0 = 6.0$ mm; $U_0 = 612$ m/s; $T_0 = 725$ K;

The MTS model parameters for the R_c 30 temper of 4340 steel have been discussed

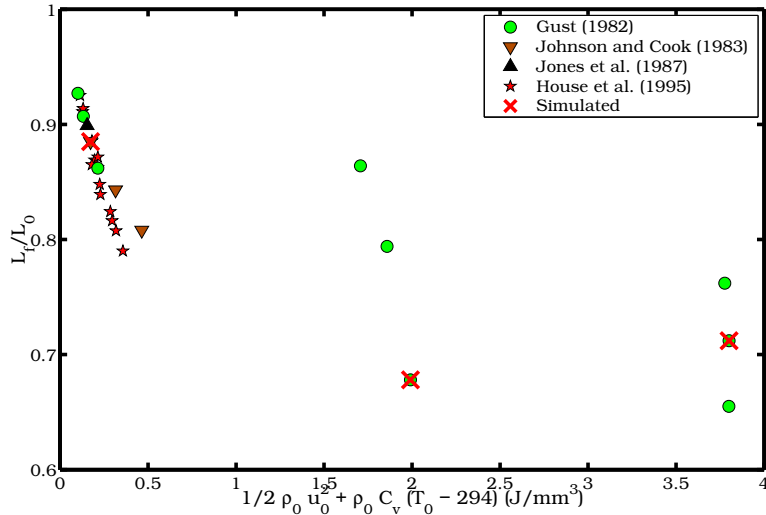


Fig. 28. The ratio of the final length to the initial length of Taylor impact specimens as a function of initial energy density. The experimental data are from Gust [17], Johnson and Cook [23], Jones and Gillis [25], and House et al. [21]. The tests that we have simulated are marked with crosses.

earlier. The MTS parameters for the R_c 40 temper of 4340 steel can either be calculated using the linear fit for various hardness levels (shown in Figure 9) or by a linear interpolation between the R_c 38 and the R_c 45 values. MTS model parameters at temperatures above 1040 K take the high temperature values discussed earlier. The initial yield stress in the Johnson-Cook model is obtained from the R_c - σ_0 relation discussed earlier. The computed final profiles are compared with the experimental data in Figures 29(a), (b), (c), and (d).

For the room temperature test (Figure 29(a)), the Johnson-Cook model accurately predicts the final length, the mushroom diameter, and the overall profile. The MTS model underestimates the mushroom diameter by 0.25 mm. This difference is within experimental variation (see House et al. [21]).

The simulations at 725 K (Figure 29(b)) overestimate the final length of the specimen. The legend shows two MTS predictions for this case - MTS (1) and MTS (2). MTS (1) uses parameters σ_i and g_{0i} that have been obtained using the fits shown in Figure 9. MTS (2) used parameters obtained by linear interpolation between the R_c 38 and R_c 45 values. The MTS (2) simulation predicts a final length that is slightly less than that predicted by the MTS (1) and Johnson-Cook models. The mushroom diameter is also slightly larger for the MTS (2) simulation.

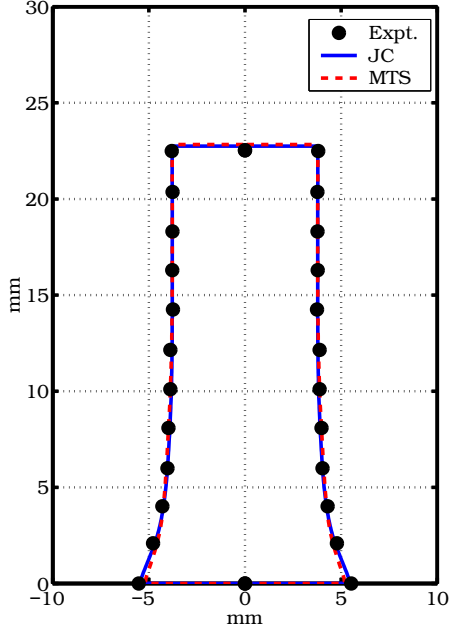
The final length of the specimen for Case 2 is not predicted accurately by either model. We have confirmed that this error is not due to discretization. Volumetric locking does not occur with the numerical method used (the explicit Material Point Method). In the absence of more high temperature Taylor impact data it is unclear if the error is within experimental variation. The final mushroom diameter is not provided by [17]. However, the author mentions that no fracture was observed in the specimen. Hence, a smaller final length due to fracture of the base can be discounted.

The third case (Figure 29(c)) was simulated at an initial temperature of 1285 K (above the α - γ phase transition temperature of iron). The MTS and Johnson-Cook models predict almost exactly the same behavior for this case. The final length is overestimated by both the models. Notice that the final lengths shown in Figure 28 at or near this temperature and for similar initial velocities vary from 0.65 to 0.75 of the initial length. The simulations predict a final length that is approximately 0.77 times the initial length - which is to the higher end of the range of expected final lengths. The discrepancy may be because the models do not predict sufficient strain hardening at these high temperatures.

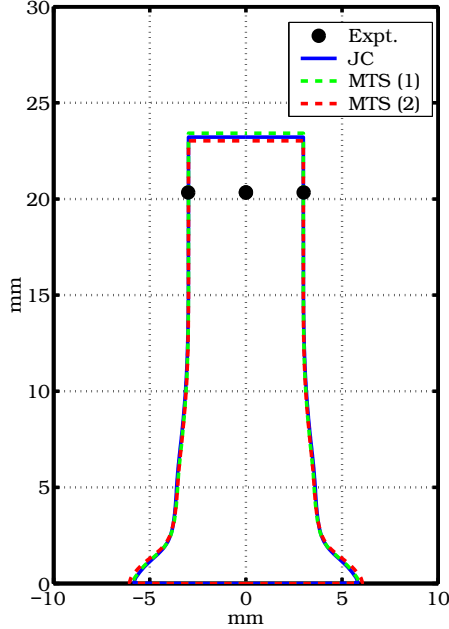
In all three cases, the predictions from the MTS and the Johnson-Cook models are nearly identical. To determine if any significant difference between the predictions of these models can be observed at higher strain rates, we simulated the geometry of Case 2 with a initial velocity of 612 m/s. The resulting profiles predicted by the MTS and the Johnson-Cook models are shown in Figure 29(d). In this

case, the MTS model predicts a slightly wider mushroom than the Johnson-Cook model. The final predicted lengths are almost identical. Interestingly, the amount of strain hardening predicted by the MTS model is smaller than that predicted by the

$L_0 = 25.4 \text{ mm}; D_0 = 7.62 \text{ mm}; U_0 = 208 \text{ m/s}; T_0 = 298 \text{ K}$ $L_0 = 30 \text{ mm}; D_0 = 6 \text{ mm}; U_0 = 312 \text{ m/s}; T_0 = 725 \text{ K}$

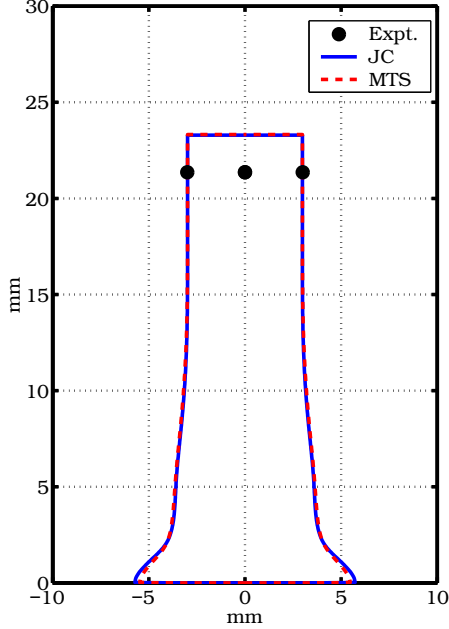


(a) Case 1.



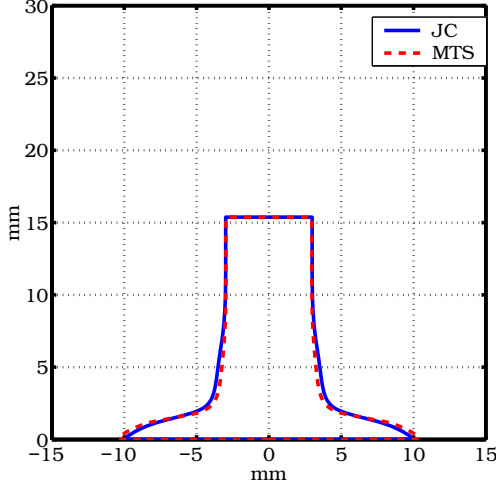
(b) Case 2.

$L_0 = 30 \text{ mm}; D_0 = 6 \text{ mm}; U_0 = 160 \text{ m/s}; T_0 = 1285 \text{ K}$



(c) Case 3.

$L_0 = 30 \text{ mm}; D_0 = 6 \text{ mm}; U_0 = 612 \text{ m/s}; T_0 = 725 \text{ K}$



(d) Case 4.

Fig. 29. Comparison of MTS and JC predictions of final Taylor specimen profiles with experimental results.

Johnson-Cook model (as can be observed from the secondary bulge in the cylinder above the mushroom). We conclude that the Johnson-Cook and MTS models presented in this paper predict almost identical elastic-plastic behavior in the range of conditions explored. Please note that quite different sets of data were used to determine the parameters of these models and hence the similarity of the results indicate the underlying accuracy of the parameters.

7 Remarks and Conclusions

We have determined parameters for the Mechanical Threshold Stress model and the Johnson-Cook model for various tempers of 4340 steel. The predictions of the MTS model have been compared with experimental stress-strain data. Yield stresses predicted by the Johnson-Cook and the MTS model have been compared for a range of strain rates and temperatures. Taylor impact tests have been simulated and the predicted profiles have been compared with experimental data.

Some remarks and conclusions regarding this work are given below.

- (1) The MTS and Johnson-Cook models predict similar stress-strain behaviors over a large range of strain rates and temperatures. Noting that the parameters for these models have been obtained from different sets of experimental data, the similarity of the results, especially in the Taylor test simulations, is remarkable. We suggest that this is an indication of the accuracy of the models and the simulations.
- (2) The MTS model parameters are considerably easier to obtain than the Johnson-Cook parameters. However, the MTS simulations of the Taylor impact tests take approximately 1.5 times longer than the Johnson-Cook simulations. This is partly because the shear modulus and melting temperature models are not evaluated in the Johnson-Cook model simulations. Also, the MTS model involves more floating point operations than the Johnson-Cook model. The Johnson-Cook model is numerically more efficient than the MTS model and would be preferable for large numerical simulations involving 4340 steel.
- (3) The Nadal-LePoac shear modulus model and the Burakovsky-Preston-Silbar melting temperature model involve less data fitting and are the suggested models for elastic-plastic simulations over a large range of temperatures and strain rates. The specific heat model that we have presented leads to better predictions of the rate of temperature increase close to the α - γ phase transition of iron. The shear modulus and melt temperature models are also valid in the range of strain rates of the order of 10^8 /s. The Mie-Grüneisen equation of state should probably be replaced by a higher order equation of state for extremely high rate processes.
- (4) The relations between the Rockwell C hardness and the model parameters that have been presented provide reasonable estimates of the parameters. However,

more data for the R_c 30, 45, and 49 tempers are needed for better estimates for intermediate tempers. There is an anomaly in the strain rate and temperature dependence of the yield strength for R_c 50 and higher tempers of 4340 steel. We would suggest that the values for R_c 49 steel be used for harder tempers. For tempers below R_c 30, the fits discussed earlier provide reasonable estimates of the yield stress.

- (5) The strain hardening (Voce) rule in the MTS model may be a major weakness of the model and should be replaced with a more physically based approach. The experimental data used to determine the strain hardening rate parameters appear to deviate significantly from Voce behavior in some cases.
- (6) The determination of the values of g_{0es} and σ_{es0} involves a Fisher type modified Arrhenius plot. We have observed that the experimental data for the R_c 45 and R_c 49 tempers do not tend to reflect an Arrhenius relationship. More experimental data (and information on the variation of the experimental data) are required to confirm this anomaly and is beyond the scope of this work.
- (7) The superiority of the MTS model for simulating 4340 steel is not as obvious as it is for OFHC copper and Tantalum-Tungsten alloys. More experimental strain-strain and Taylor impact data at high temperatures and high strain rates are needed to confirm this observation.

Acknowledgments

This work was supported by the the U.S. Department of Energy through the Center for the Simulation of Accidental Fires and Explosions, under grant W-7405-ENG-48.

REFERENCES

- [1] Bancroft, D., Peterson, E. L., Minshall, S., 1956. Polymorphism of iron at high pressure. *J. Appl. Phys* 27 (3), 291–298.
- [2] Banerjee, B., 2005. Simulation of impact and fragmentation with the material point method. In: *Proc. 11th International Conference on Fracture*. Turin, Italy.
- [3] Banerjee, B., 2005. Validation of UINTAH: Taylor impact and plasticity models. In: *Proc. 2005 Joint ASME/ASCE/SES Conference on Mechanics and Materials (McMat 2005)*. Baton Rouge, LA.
- [4] Barker, L. M., Hollenbach, R. E., 1974. Shock wave study of the $\alpha \rightleftharpoons \epsilon$ phase transition in iron. *J. Appl. Phys.* 45 (11), 4872–4887.
- [5] Brown, J. M., Fritz, J. N., Hixson, R. S., 2000. Hugoniot data for iron. *J. Appl. Phys.* 88 (9), 5496–5498.
- [6] Brown, W. F., Mindlin, H., Ho, C. Y., 1996. *Aerospace Structural Metals*

- Handbook: Volume 1: Code 1206. CINDAS/USAF CRDA Handbooks Operation, Purdue University, West Lafayette, IN.
- [7] Burakovsky, L., Preston, D. L., 2000. Analysis of dislocation mechanism for melting of elements. *Solid State Comm.* 115, 341–345.
 - [8] Burakovsky, L., Preston, D. L., Silbar, R. R., 2000. Analysis of dislocation mechanism for melting of elements: pressure dependence. *J. Appl. Phys.* 88 (11), 6294–6301.
 - [9] Burakovsky, L., Preston, D. L., Silbar, R. R., 2000. Melting as a dislocation-mediated phase transition. *Phys. Rev. B* 61 (22), 15011–15018.
 - [10] Chen, S. R., Gray, G. T., 1996. Constitutive behavior of tantalum and tantalum-tungsten alloys. *Metall. Mater. Trans. A* 27A, 2994–3006.
 - [11] Chi, Y. C., Lee, S., Cho, K., Duffy, J., 1989. The effect of tempering and test temperature on the dynamic fracture initiation behavior of an AISI 4340 VAR steel. *Mat. Sci. Eng. A114*, 105–126.
 - [12] Follansbee, P. S., Kocks, U. F., 1988. A constitutive description of the deformation of copper based on the use of the mechanical threshold stress as an internal state variable. *Acta Metall.* 36, 82–93.
 - [13] Fukuhara, M., Sanpei, A., 1993. Elastic moduli and internal friction of low carbon and stainless steels as a function of temperature. *ISIJ International* 33 (4), 508–512.
 - [14] Goto, D. M., Bingert, J. F., Chen, S. R., Gray, G. T., Garrett, R. K., 2000. The mechanical threshold stress constitutive-strength model description of HY-100 steel. *Metallurgical and Materials Transactions A* 31A, 1985–1996.
 - [15] Goto, D. M., Bingert, J. F., Reed, W. R., Garrett, R. K., 2000. Anisotropy-corrected MTS constitutive strength modeling in HY-100 steel. *Scripta Mater.* 42, 1125–1131.
 - [16] Guinan, M. W., Steinberg, D. J., 1974. Pressure and temperature derivatives of the isotropic polycrystalline shear modulus for 65 elements. *J. Phys. Chem. Solids* 35, 1501–1512.
 - [17] Gust, W. H., 1982. High impact deformation of metal cylinders at elevated temperatures. *J. Appl. Phys.* 53 (5), 3566–3575.
 - [18] Gust, W. H., Steinberg, D. J., Young, D. A., 1979. Hugoniot parameters to 320 GPa for three types of steel. *High Temp. High Pres.* 11, 271–280.
 - [19] Handbook, A., 1978. *American Society of Metals Handbook: Volume 1.* American Society of Metals, New York.
 - [20] Hanson, K. M., 2005. Inference about the plastic behavior of materials from experimental data. In: Hanson, K. M., Hemez, F. M. (Eds.), *Sensitivity Analysis of Model Output.* Los Alamos Research Library, Los Alamos, NM, pp. 126–136.
 - [21] House, J. W., Lewis, J. C., Gillis, P. P., Wilson, L. L., 1995. Estimation of the flow stress under high rate plastic deformation. *Int. J. Impact Engng.* 16 (2), 189–200.
 - [22] Jansen, H. J. F., Hathaway, K. B., Freeman, A. J., 1984. Structural properties of ferromagnetic bcc iron: A failure of the local-spin-density approximation. *Phys. Rev. B* 30 (10), 6177–6179, lattice constant for bcc iron.

- [23] Johnson, G. R., Cook, W. H., 1983. A constitutive model and data for metals subjected to large strains, high strain rates and high temperatures. In: Proc. 7th International Symposium on Ballistics. pp. 541–547.
- [24] Johnson, G. R., Cook, W. H., 1985. Fracture characteristics of three metals subjected to various strains, strain rates, temperatures and pressures. *Int. J. Eng. Fract. Mech.* 21, 31–48.
- [25] Jones, S. E., Gillis, P. P., 1987. On the equation of motion of the undeformed section of a Taylor impact specimen. *J. Appl. Phys.* 61 (2), 499–502.
- [26] Katz, S., Doran, D. G., Curran, D. R., 1959. Hugoniot equation of state of aluminum and steel from oblique shock measurements. *J. Appl. Phys.* 30 (4), 568–576.
- [27] Kocks, U. F., 2001. Realistic constitutive relations for metal plasticity. *Materials Science and Engrg.* A317, 181–187.
- [28] Larson, F. R., Nunes, J., 1961. Low temperature flow and fracture tension properties of heat treated SAE 4340 steel. *Trans. ASM* 53, 663–682.
- [29] Lederman, F. L., Salamon, M. B., Shacklette, L. W., 1974. Experimental verification of scaling and test of the universality hypothesis from specific heat data. *Phys. Rev. B* 9 (7), 2981–2988.
- [30] Lee, W.-S., Yeh, G.-W., 1997. The plastic deformation behavior of AISI 4340 alloy steel subjected to high temperature and high strain rate loading conditions. *J. Mater. Proc. Tech.* 71, 224–234.
- [31] McQueen, R. G., Marsh, S. P., Taylor, J. W., Fritz, J. N., Carter, W. J., 1970. The equation of state of solids from shock wave studies. In: Kinslow, R. (Ed.), *High Velocity Impact Phenomena*. Academic Press, New York, pp. 294–417.
- [32] Nadal, M.-H., Le Poac, P., 2003. Continuous model for the shear modulus as a function of pressure and temperature up to the melting point: analysis and ultrasonic validation. *J. Appl. Phys.* 93 (5), 2472–2480.
- [33] Nicholas, T., 1981. Tensile testing of materials at high rates of strain. *Experimental Mechanics* 21, 117–185.
- [34] Ravichandran, G., Rosakis, A. J., Hodowany, J., Rosakis, P., 2001. On the conversion of plastic work into heat during high-strain-rate deformation. In: Proc. , 12th APS Topical Conference on Shock Compression of Condensed Matter. American Physical Society, pp. 557–562.
- [35] Shacklette, L. W., 1974. Specific heat and resistivity of iron near its Curie point. *Phys. Rev. B* 9 (9), 3789–3792.
- [36] Steinberg, D. J., Cochran, S. G., Guinan, M. W., 1980. A constitutive model for metals applicable at high-strain rate. *J. Appl. Phys.* 51 (3), 1498–1504.
- [37] Tanimura, S., Duffy, J., 1986. Strain rate effects and temperature history effects for three different tempers of 4340 VAR steel. *Int. J. Plasticity* 2, 21–35.
- [38] Varshni, Y. P., 1970. Temperature dependence of the elastic constants. *Physical Rev. B* 2 (10), 3952–3958.
- [39] Wallace, D. C., Sidles, P. H., Danielson, G. C., 1960. Specific heat of high purity iron by a pulse heating method. *J. Appl. Phys.* 31 (1), 168–176.
- [40] Wilkins, M. L., 1999. *Computer Simulation of Dynamic Phenomena*. Springer-Verlag, Berlin.

- [41] Williams, Q., Jeanloz, R., Bass, J., Svendsen, B., Ahrens, T. J., 1987. The melting curve of iron to 250 gigapascals: a constraint of the temperature at earth's center. *Science* 236, 181–182.
- [42] Yoo, C. S., Holmes, N. C., Ross, M., 1993. Shock temperatures and melting of iron at earth core conditions. *Phys. Rev. Lett.* 70 (25), 3931–3934.
- [43] Zocher, M. A., Maudlin, P. J., Chen, S. R., Flower-Maudlin, E. C., 2000. An evaluation of several hardening models using Taylor cylinder impact data. In: *Proc. , European Congress on Computational Methods in Applied Sciences and Engineering. ECCOMAS, Barcelona, Spain.*